EurJOC
European Journal of Organic Chemistry

Review
doi.org/10.1002/ejoc.202101428

Chemistry Europe
European Chemical Societies Publishing

www.eurjoc.org

Special Collection

π-Extended *peri*-Acenes: Recent Progress in Synthesis and Characterization

M. R. Ajayakumar,[a] Ji Ma,*[a] and Xinliang Feng*[a, b]

In memory of François Diederich.

Nanographenes (NGs) with open-shell character have gained intense attention due to their potential applications in future organic nanoelectronics and spintronics. Among them, NGs bearing a pair of parallel zigzag edges, such as acenes and *peri*-acenes (PAs) bestow unique (opto)electronic and magnetic properties owing to their localized non-bonding π-state. However, their reactive zigzag edges impart intrinsic instability, leading to the challenging synthesis. The recent development of synthetic strategies provided access to several π-extended PAs, which were considered unrealistic for decades. Notably, their laterally π-extended structures of zigzag-edged graphene nanoribbons was realised via on-surface synthesis. However, synthesis of π-extended PAs in solution is still in its infancy, more intensive scientific efforts are needed to surpass the existing challenges regarding stability and solubility. This Review provides an overview of recent progress in the synthesis and characterization of PAs through a bottom-up synthetic strategy, including on-surface and solution-phase chemistry. In addition, views on existing challenges and the future prospects are also provided.

1. Introduction

The structurally confined nanoscale graphene fragments, namely nanographenes (NGs) are considered to be promising candidates for next-generation semiconductor materials because they possess defined and finite bandgaps.[1–4] According to their size sale, NGs can be classified as graphene molecules, graphene nanoribbons and graphene quantum dots.[5] The electronic and physicochemical properties of NGs are exquisitely sensitive to their size, shape and edge structures.[6–8] Typically, NGs have three representative types of edge structures, including armchair, zigzag, and cove (Figure 1).[9] The NGs bearing armchair or cove edges usually manifest semiconducting properties, while the zigzag-edged NGs are associated with remarkable spin-polarization, referred as "edge state", due to the multi-electron correlation of unpaired electrons present on the zigzag edges.[6] Therefore, the zigzag-edged NGs feature non-trivial π-magnetism and open the avenues towards molecular spintronics.[10–11] For example, Tanaka et al.[12] theoretically predicted that the zigzag-edged graphene nanoribbons (ZGNRs) comprise the highly edge-localized nonbonding orbitals by using a tight-binding calculation method. With increase in the length of ZGNRs, the bandgaps decreased rapidly and the wave functions completely localized over its edges at the Fermi level. Intrigued by the theoretical studies, enormous efforts towards the synthesis of ZGNRs and its "finite" models have been dedicated by the materials scientists and chemists via either "top-down" or "bottom-up" methods.[2,5,13] The "top-down" approaches typically comprises the lithographical scission of graphene sheets, the "unzipping" of carbon nanotubes, and plasma etching, etc. However, these methods suffer from several limitations, such as poor atomic precision, structural defects, and low yields, etc., resulting in the poorly defined bandgaps of NGs. In contrast, the "bottom-up" approaches, such as the surface-assisted synthesis and solution-mediated synthesis, allow for precise control of the size and edge structures of NGs at the atomic level, which enables the fine tuning of their bandgaps and opto-electronic properties.[2,14–16] Thanks to the development of modern synthetic methods and

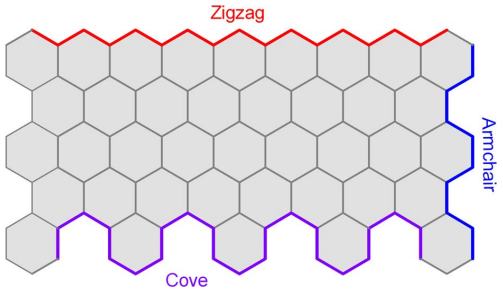

Figure 1. The representative edge structures of nanographenes.

[a] Dr. M. R. Ajayakumar, Dr. J. Ma, Prof. Dr. X. Feng
Center for Advancing Electronics Dresden (cfaed)
and Faculty of Chemistry and Food Chemistry,
Technische Universität Dresden
Mommsenstrasse 4, 01062 Dresden, Germany
E-mail: ji.ma@tu-dresden.de
xinliang.feng@tu-dresden.de
https://tu-dresden.de/mn/chemie/mc/mc2/die-professur
[b] Prof. Dr. X. Feng
Department of Synthetic Materials and Functional Devices,
Max Planck Institute of Microstructure Physics
Weinberg 2, Halle (Saale), 06120 Germany

Special Collection *This article belongs to a Joint Special Collection dedicated to François Diederich.*

advanced analytical tools, several types of atomically precise zigzag-edged NGs consisting of acenes[17], *peri*-acenes (PAs), *peri*-acenoacenes, zethrenes, circumacenes, triangulenes, *etc.*, have been recently synthesized and characterized, in view of their intriguing open-shell characters and potential applications in carbon-based nanoelectronics and spintronics.[16–26]

The research in our group mainly focuses on the precision synthesis of graphene nanostructures with structurally well-defined topologies and on the exploration of their exotic electronic and magnetic properties.[16,27–30] Among them, the chemistry of PAs has been a longstanding research interest in our group. In this review, we will highlight recent advances in the synthetic strategies and characterization methods towards π-extended PAs through both on-surface and solution-phase syntheses by our group and others. The advantages and challenges of the respective rational molecular design and synthetic routes will be discussed in this context, including the different stabilization strategies (i.e., introduction of bulky or electron-deficient substitutions) for the solution-synthesized π-extended PAs. In addition, the synthesis and properties of heteroatom-doped PAs will be discussed in comparison with their all-carbon counterparts. Furthermore, the discussion on the synthesis of PA-based GNRs and PA-bridged cumulene polymers as well as their unique electronic, and magnetic properties will be also provided.

2. *peri*-Acenes (PAs)

[n]Acenes (*or commonly acenes*), which are composed of linearly fused benzene rings with general formula $C_{4N+2}H_{2N+4}$, have long been the intense research subject due to the unique opto-electronic properties associated with their π-conjugated topology.[31,32] They have the narrowest energy gaps (ΔE_g), i.e., HOMO-LUMO gap, among the polycyclic aromatic hydrocarbons (PAHs) of comparable size and the ΔE_g decreases with increase in molecular length.[33] The small HOMO–LUMO gap in larger acenes than hexacene would result in approximately degenerate frontier orbitals, giving the emergence of an open-shell singlet ground state (Figure 2a).[34,35] This phenomenon can also be demonstrated by Clar's aromatic π-sextet rule, which states that the resonance form with the maximum number of π-sextets determines the electronic ground state.[36]

Peri-condensation of acenes (Figure 2b) gives the rectangular PAHs comprising 'm' rows of *peri*-fused [n]acenes, and thus can be also referred to as [n,m]*peri*-acene (or [n,m]PA).[37,38] As the conjugation is extended to a certain point, a prominent diradical character may emerge which originates from a narrow bandgap and stabilization through recovery of Clar's sextet in the open-shell resonance form. Like acenes, PAs also possess attractive electronic and magnetic properties by virtue of the rich zigzag edges and have been considered as the ideal finite-size models for investigating the edge states of ZGNRs.[39,40] The PAs have been extensively investigated with quantum chemical calculations and their prominent open-shell ground states were predicted with increase in the length of zigzag edges.[40–44] The evolution of diradical (or multiradical) character in PAs with extension of zigzag edges is more rapid than acenes. Kubo and co-workers[45] defined the degree of ground state open-shell behaviour (y_i) of PAs using Yamaguchi scheme[46,47] combined with symmetry-broken UBHandHLYP/6-31G* level of theory. The y_i can be calculated using the equation: $y_i = 1-2T_i/(1+T_i^2)$, $T_{i=}(n_{HOMO-i}-n_{LUMO+i})/2$, where n_{HOMO-i} and n_{LUMO+i} represent the natural orbital occupation numbers of HOMO−i and LUMO+i,

M. R. Ajayakumar obtained his PhD from Jawaharlal Nehru University (India) in 2013, and then joined Institut de Ciència de Materials de Barcelona (Spain) for his first postdoctoral research. Currently, he is working as a postdoctoral researcher at the Chair of Molecular Functional Materials, Technische Universität Dresden. His current research interests are the bottom-up synthesis, characterization, and applications of functional organic molecules, such as polyaromatic hydrocarbons, open-shell nanographenes, and graphene nanoribbons.

Ji Ma received his PhD degree in synthetic chemistry under the supervision of Prof. Xinliang Feng from Technische Universität Dresden in 2019. In the same year, he was appointed as a research group leader at the Chair of Molecular Functional Materials at the Technische Universität Dresden. His research interests are the precision synthesis of novel aromatic compounds, nanographenes, graphene nanoribbons, and heteroatom-doped carbon nanostructures as well as their applications in organic nanoelectronics and the emerging organic spintronic fields.

Xinliang Feng has been full professor and the head of the Chair of Molecular Functional Materials at Technische Universität Dresden since 2014. Starting from 2021, he has been the director of Max Planck Institute of Microstructure Physics (Halle), Germany. His current scientific interests include organic synthesis, supramolecular chemistry of π-conjugated systems, bottom-up synthesis and top-down fabrication of graphene and graphene nanoribbons, 2D polymers and supramolecular polymers, as well as 2D carbon-rich conjugated polymers for (opto)electronic applications and materials for energy storage and conversion.

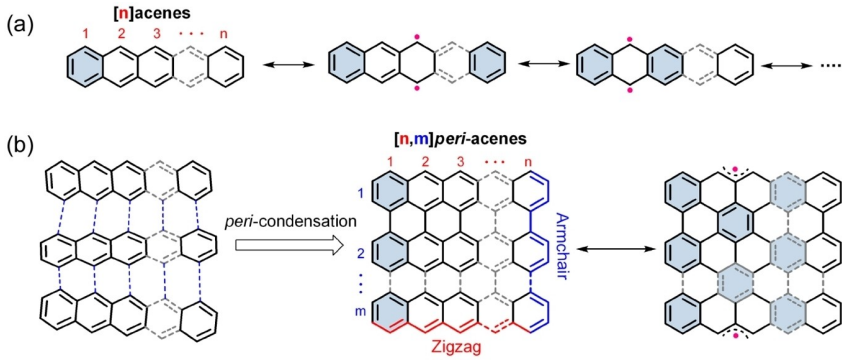

Figure 2. Chemical structure and respective open-shell resonance structures of [n]acenes and [n,m]*peri*-acenes.

respectively. The ground state singlet diradical character (y_0) and tetraradical character (y_1), which are related to the first and second π-bond cleavages, respectively, can vary from 0 to 1 according to the degree of open-shell nature. As shown in the Table 1, the y_0 of [3,2]PA (namely, bisanthene) is 0.12, which is basically classified as a closed-shell molecule. However, a higher analogue [3,3]PA (i.e., teranthene) shows $y_0 = 0.59$, indicating its noticeable singlet diradical character. The larger analogues give larger y_0, indicating their appreciable diradical feature. For molecule with a large value of y_1, the diradical description is incomplete and the tetraradical nature needs to be taken into account. For example, the y_1 of [6,3]PA is 0.44, suggesting that the tetraradical character becomes prominent for higher order PAs. In addition, the evolution of open-shell behaviour of PAs can also be explained based on Clar's sextet theory (Figure 2b). The molecular structures of PAs can be drawn as a resonance hybrid of closed-shell and open-shell forms and the contribution from the open-shell forms would be dominant when the difference in the number of Clar's sextet between the closed-shell and open-shell form is more than two.

The [2,2]PA (perylene) and [3,2]PA (bisanthene) are closed-shell PAs, which were reported for the first time by Scholl and co-workers in the early 20th century.[48–50] Since then, both perylene and bisanthene have become attractive molecular scaffolds in organic materials chemistry.[51–53] The longitudinally extended perylenes such as [2,3]PA (terrylene; $\Delta E_g = 2.1$ eV) and [2,4]PA (quaterrylene; $\Delta E_g = 1.8$ eV) were synthesised based on alkali metal-induced cyclization of oligonaphthalene precursors, which were characterised as closed-shell molecules.[54] These rylene molecules and their imide derivatives were extensively explored in the pursuit of stable dyes with excellent NIR absorbance/fluorescence and high extinction coefficients.[55,56] The higher PAs ($n \geq 3$ and $m \geq 3$; $n \geq 4$ and $m = 2$) are theoretically predicted to show open-shell character, and hence, the synthesis of π-extended PAs are highly challenging.

In 2010, Kubo et al. provided the first experimental evidence for the open-shell nature of PAs by realising the kinetically protected [3,3]PA (i.e. teranthene **7**).[57] As shown in Figure 3, a partial cyclisation of the teranthrylene derivative **1** with KOH/quinoline (dehydrochlorination) and a full cyclization with DDQ/$Sc(OTf)_3$ at high temperature were the key steps. By following identical synthetic approach of [3,3]PA, they also succeeded in the synthesis of the higher analogue [3,4]PAs (i.e. quateranthenes **8a** and **8b**) from the corresponding anthrylene derivative **2**.[58] To render substantial solubility and kinetic stability, they incorporated *tert*-butyl and mesityl groups to the reactive edge positions. The teranthene **7** was isolated as dark green crystals (Figure 4a) upon evaporation of its CH_2Cl_2/hexane solution under an argon flow. The half-life time ($t_{1/2}$) of **7** in toluene was estimated as 3 days upon exposure to air under ambient conditions. The single crystals of quateranthene **8a** were obtained from its o-dichlorobenzene/mesitylene solution in a sealed degassed tube at 3 °C. However, the **8a** is less stable ($t_{1/2} = 15$ h) compared to **7** under ambient conditions. The CD_2Cl_2 solutions of these teranthene and quateranthene derivatives did not show ^{1}H NMR signals corresponded to the aromatic core at room temperature, indicating the presence of thermally populated triplet species. Upon cooling, progressive line sharpening was observed for **7** (Figure 4b) whereas the no change was observed for **8b** even at −92 °C. This result was attributed to the smaller singlet–triplet energy gaps ($\Delta E_{S\text{-}T}$) of **8b** compared to **7** which caused the large population of the thermally excited triplet species even at low temperatures. The powder samples of **7** and **8b** were submitted for superconducting quantum interference device (SQUID) measurements and the $\Delta E_{S\text{-}T}$ were estimated as −16.0 kJ/mol and −2.9 kJ/mol, respectively. These substantially small $\Delta E_{S\text{-}T}$ values evidenced the very weak coupling of electrons and the edge localization of unpaired electrons. The optical energy gaps

Table 1. The calculated singlet diradical character and tetraradical character (y_0, y_1) of [n,m]PA (UBHandHLYP/6-31G* calculation).[45]

n m	2	3	4	5	6	7
1	(0.00, 0.00)	(0.00, 0.00)	(0.01, 0.01)	(0.07, 0.00)	(0.20, 0.01)	(0.40, 0.02)
2	(0.00, 0.00)	(0.12, 0.00)	(0.60, 0.01)	(0.84, 0.02)	(0.94, 0.07)	(0.98, 0.20)
3	(0.01, 0.00)	(0.59, 0.00)	(0.91, 0.01)	(0.98, 0.05)	(0.99, 0.23)	(1.00, 0.54)
4	(0.05, 0.00)	(0.84, 0.00)	(0.98, 0.01)	(1.00, 0.10)	(1.00, 0.44)	(1.00, 0.77)

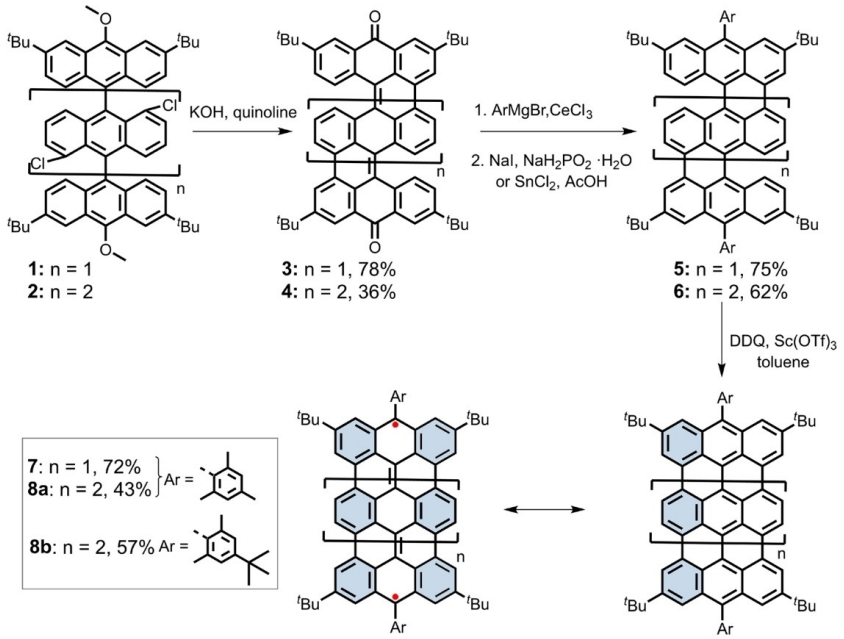

Figure 3. Synthesis of teranthene (**7**) and quateranthene (**8**).

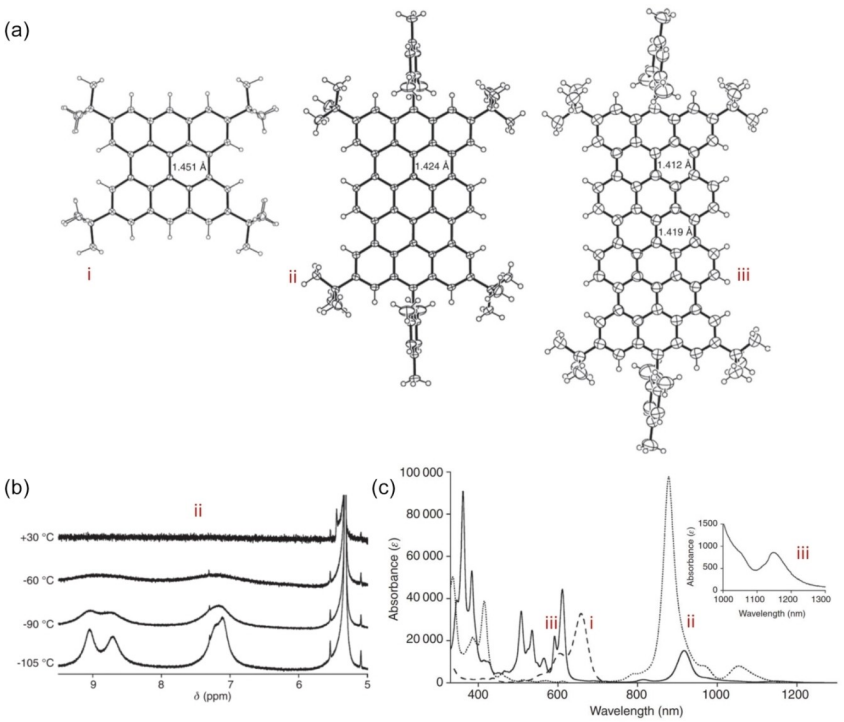

Figure 4. (a) Crystal structures of *t*-butyl substituted (i) bisanthene, (ii) teranthene **7**, and (iii) quateranthene **8 a**. (b) Variable-temperature ^{1}H NMR spectra of **7** in CD_2Cl_2 in the aromatic region. (c) One-photon electronic absorption spectra of *t*-butyl substituted bisanthene (i), teranthene **7** (ii), and quateranthene **8 b** (iii). The inset indicates the weak band of **8 b** beyond 1000 nm. Reproduced from Ref. [59] Copyright (2014), with permission from De Gruyter.

(Figure 4c) of **7** ($\Delta E_g = 1.18$ eV) is 0.64 eV smaller than that of bisanthene ($\Delta E_g = 1.82$ eV), but comparable to **8 b** ($\Delta E_g =$ 1.08 eV).[59]

Similar to the longitudinal extension of bisanthene, the lateral extension also induces open-shell ground states. The difference in the number of Clar sextets between the diradical and the Kekulé form is three for the laterally extended larger [n,2]PAs, such as [4,2]PA (namely *peri*-tetracene), [5,2]PA (*peri*-pentacene) and [7,2]PA (*peri*-heptacene). As an initial attempt towards the elusive *peri*-tetracene ([4,2]PA) synthesis, our group

first reported a partially fused [4,2]PA, namely bistetracene (**12**) (Figure 5a), where two tetracenes are fused together by two bonds.[60] The key dialdehyde-precursor **9** was synthesized in eight steps from the commercially available 1,4-dibromo-2,5-diiodobenzene. After that, the target compound **12** was synthesized from **9** through successive Grignard reaction, Friedel–Crafts alkylation, and oxidative dehydrogenation in 60% yield in three steps. The singlet diradical ground state (y_0 = 0.61) was proved by the line sharpening effect of ^{1}H NMR signals upon cooling and the intensity increase of electron paramagnetic resonance (EPR) signal (Figure 5c) with increase in temperature ($\Delta E_{S\text{-}T} = -3.4$ kcal/mol). The optical energy gap of bistetracene **12** was estimated to be 1.56 eV based on UV-vis absorption spectroscopy. Moreover, the unstable **12** ($t_{1/2}$ = 30 min) was oxidized to the corresponding dione **13** (Figure 5a, Figure 5b) under ambient conditions. Recently, a reasonably simple synthetic approach was developed by Adachi et al. for the bistetracenes **16** and **17** via a two- or three-step reaction strategy (Figure 6a) in low yield from tetracen-5(12*H*)-one (**14**).[61] The stability of the bistetracene can be enhanced dramatically by using bulky aryl substituents such as mesityl groups at the zigzag position, where there is no significant degradation observed even after 2 weeks under ambient conditions (Figure 6b, Figure 6c). In view of its higher stability, the semiconducting property of bis-tetracene **17c** was also demonstrated. The organic field-effect transistors (OFETs) fabricated with **17c** showed bipolar transport properties and the hole and electron mobilities were found to be 1.6×10^{-3} and 6.1×10^{-5} cm^2 V^{-1} s^{-1}, respectively.

In 2018, the kinetically protected [4,2]PA (or *peri*-tetracene) was independently synthesized in solution by us[62] and by Wu's group,[63] which represents a big step towards the solution synthesis of open-shell PAs. As shown in Figure 7, the stable key dihydro precursor was synthesised by five-step reaction strategy, and the zigzag-peripheries are substituted with four bulky groups in order to render fair solubility and substantial kinetic stability to [4,2]PA. Firstly, 1,4-dibromo-2,5-diiodobenzene (**18**) was submitted to Sonagashira coupling and Suzuki coupling with suitable building blocks and later treated with ICl to obtain **22**. After successful Scholl reactions, the compounds **23** were further submitted for double nucleophilic additions and Friedel-Crafts alkylation reactions to yield the key precursors (**24**) in good yields. Dehydrogenation of precursor **24a** with 2,3-dichloro-5,6-dicyano-1,4-benzoquinone (DDQ) yielded the final [4,2]PA derivative **25a** in a quantitative yield. Conversely, the single step dehydrogenation of dihydro precursor **24b** with DDQ did not proceed due to the strong electron-withdrawing nature of the 2,6-dichlorophenyl substituents. Therefore, the precursor **24b** was firstly converted to the corresponding dianion by deprotonation with KO^{t}Bu and then in situ oxidized by *p*-chloranil to give the final product **25b** with a yield of 88%.

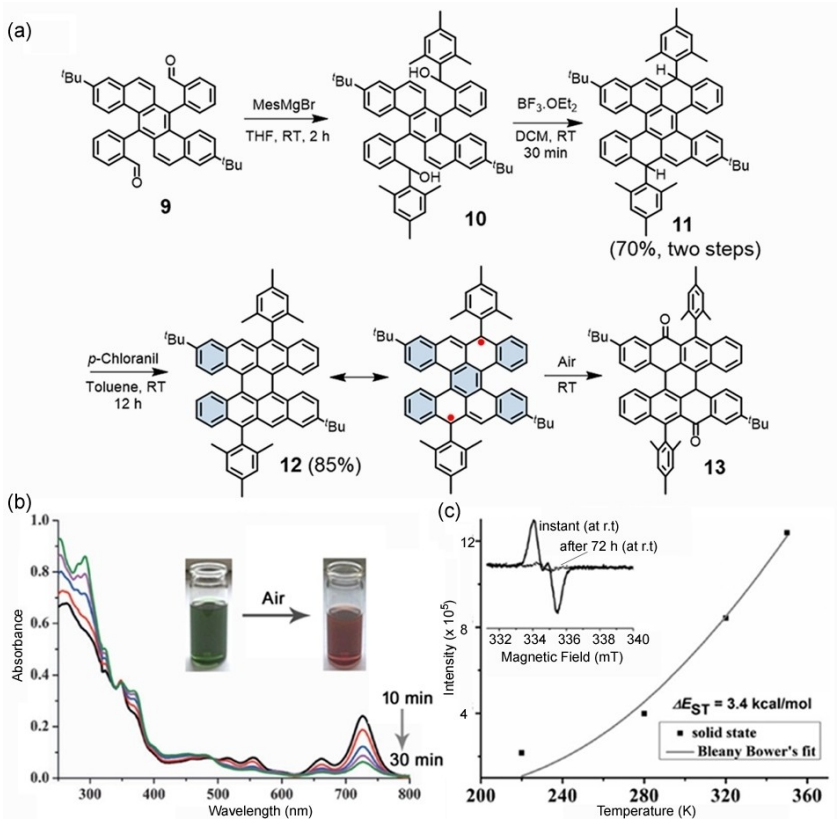

Figure 5. (a) Synthesis of bistetracene (**12**) and its decomposition under air to the corresponding dione **13**; (b) Time-dependent UV/Vis spectra of **12** under ambient conditions. (c) The change in EPR signal intensity with temperature (■) of **12** and the Bleaney-Bower's fit (solid line). Inset: EPR spectra of **12** in toluene solution at room temperature and after 72 h. Reproduced from Ref. [60].

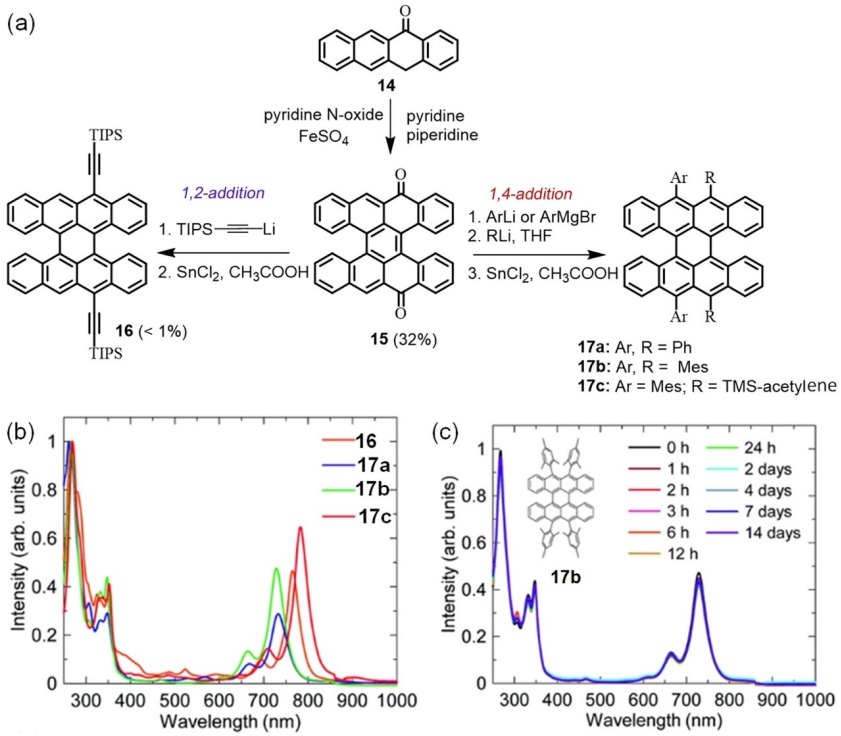

Figure 6. (a) An alternative approach for the synthesis of bistetracene derivatives (**16**–**17**). (b) UV-vis absorption spectra for bistetracene derivatives (**16**–**17**) in CH_2Cl_2. (c) UV-vis absorption spectra as a function of time for **17b**. Reproduced from Ref. [61] Copyright (2021), with permission from Royal Society of Chemistry.

The formation of **25a** and **25b** was confirmed by high resolution mass spectrometry, X-ray crystallography, EPR, and NMR analysis. As shown in Figure 8a, X-ray crystallographic analysis of **25b** combined with nucleus-independent chemical shift (NICS) calculations (Figure 8a) revealed the enhanced electronic coupling between two tetracene units. $NICS(1)_{zz}$ values of the six-membered rings linking the two tetracene moieties were less positive than that of bisanthene. Based on spin density analysis, it was proved that the zigzag C atoms with phenyl substituents possessed the highest spin densities compared to the unprotected ones. A singlet–triplet energy gap $\Delta E_{S\text{-}T}$ of -2.5 kcal mol^{-1} was obtained by fitting the SQUID data with Bleaney-Bowers equation (Figure 8b), which confirmed the open-shell singlet diradicaloid nature ($y_0 = 0.72$) of [4,2]PA. With the zigzag protection, the [4,2]PA showed remarkable persistent stability under ambient conditions ($t_{1/2} =$ 3 h for **25a**; $t_{1/2} = 7$ h for **25b**) and it could be stored in glove box for weeks. Additionally, the absorption measurements (Figure 8c) and electrochemical analysis (Figure 8d) of **25a** validated the existence of a narrow energy gap of [4,2]PA ($\Delta E_g = 1.11$ eV).

Interestingly, controlled Diels-Alder reactions of **25a** can be performed at the bay positions with suitable dienophiles, which enabled the synthesis of open-shell benzo-*peri*-tetracenes (BPTs) and closed-shell circumanthracenes (Figure 7b).[64] It was also reported that the oxidants employed for the [4,2]PA synthesis (Figure 7) such as DDQ and p-chloranil could even act as dienophiles when they were excess in the reaction mixture. Excess addition of DDQ to the dihydro-precursor **24a** triggered the in situ synthesis of **25a**, which successively underwent two-side Diels-Alder reactions with DDQ at room temperature in one-pot to generate closed-shell tetracyano-circumanthracene derivative **26** in 30% yield. The dicyano-BPT **27** was also synthesised with a yield of 20% by performing controlled one-fold Diels-Alder reaction, when **25a** was treated with 1 equiv. of DDQ.

It is also worth to mention that the synthesis of a pristine [4,2]PA on Au (111) under ultrahigh-vacuum (UHV) conditions was also demonstrated by us in the same year using 7,14-di(2-methylphenyl)benzo-[*k*]tetraphene monomer **28** as the precursor (Figure 9a).[65] The detailed structural and electronic characterization of [4,2]PA was performed via bond resolved scanning tunneling microscope (STM) and scanning tunnelling spectroscopy (STS). The apparent planar confirmation of [4,2]PA on Au(111) was confirmed by ultrahigh-resolution STM (UHR-STM) imaging using a CO functionalized STM tip (Figure 9b). The electronic property of [4,2]PA on Au(111) was examined with STS, where the differential conductance (d*I*/d*V*) spectra (Figure 9c) revealed prominent features in the density of states (DOS) at -160 mV and 190 mV, which are the positive and the negative ion resonances (PIR and NIR), respectively, deriving from the HOMO and LUMO of [4,2]PA. Therefor the HOMO-LUMO gap was estimated as 350 meV on Au surface. Moreover, the DFT calculated d*I*/d*V* maps and the experimental d*I*/d*V* maps (Figure 9d) of [4,2]PA showed excellent agreement.

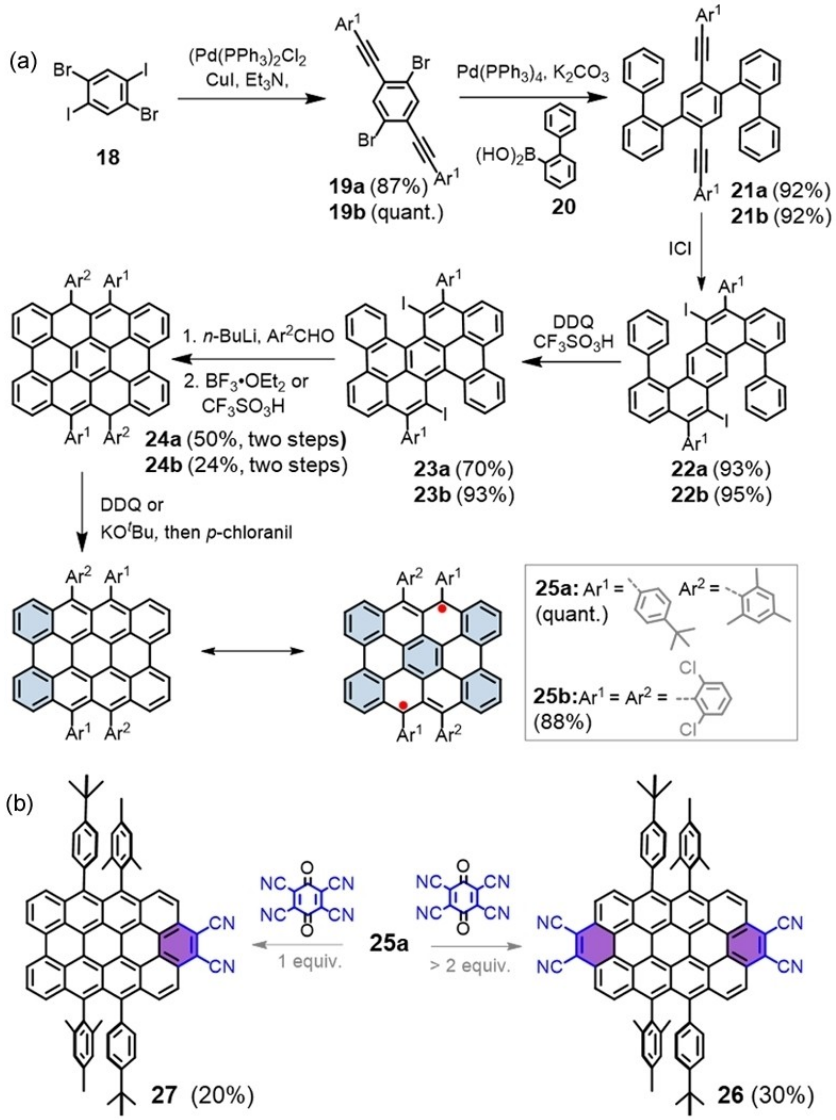

Figure 7. (a) Synthetic route towards [4,2]PA derivatives (**25a** and **25b**). (b) Controlled one-side and two-side Diels-Alder reaction of **25a** (diene) with DDQ (dienophile).

Further extension of the [4,2]PA leads to the higher homologue [5,2]PA (or *peri*-pentacene), which exhibits the larger open-shell diradical character ($y_0 = 0.84$, Table 1). However, the synthesis and isolation of [5,2]PA in solution have been unsuccessful so far although some attempts have been done by several research groups. The [5,2]PA was firstly detected as a potential side product upon thermal decomposition of pentacene, by mass spectroscopy in 2005.[66] In 2010, Wu et al.[67] synthesised a fused bispentacenequinone **30** by photocyclization of bispentacenequinone **29**. However, its conversion to zigzag substituted [5,2]PA **32** was unsuccessful due to the unusual Michael addition (Figure 10a). In 2013, Müllen et al.[68] synthesised a fully planarized *peri*-pentacene tetraketone precursor **35** as shown in Figure 10b. In this strategy, 4,5,9,10-tetrafunctionalization of pyrene was utilised to obtain a tetracyano-substituted pyrene derivative **33**, which was further submitted to Scholl reaction in presence of PIFA in order to generate the precursor **35**. However, the conversion of **35** to the respective [5,2]PA **36** was hampered by the poor solubility of the former. Therefore, the synthetic access to [5,2]PA in solution required the development of more efficient synthetic strategies, which need to circumvent the difficulties associated with the low solubility and high reactivity of [5,2]PA.

Later on, Fischer et al.[69] reported the on-surface synthesis of pristine [5,2]PA on Au(111) under UHV based on thermally induced cyclodehydrogenation of bispentacene precursor **40** (Figure 11a). The lateral fusion of pentacene units afforded rectangular flakes of [5,2]PA featuring parallel pairs of zigzag and armchair edges. The structure of [5,2]PA was confirmed by STM and atomic-resolution non-contact AFM imaging techniques (Figure 11b–d). Very recently, Écija et al.[70] synthesized [5,2]PA via on-surface reaction from a different precursor,

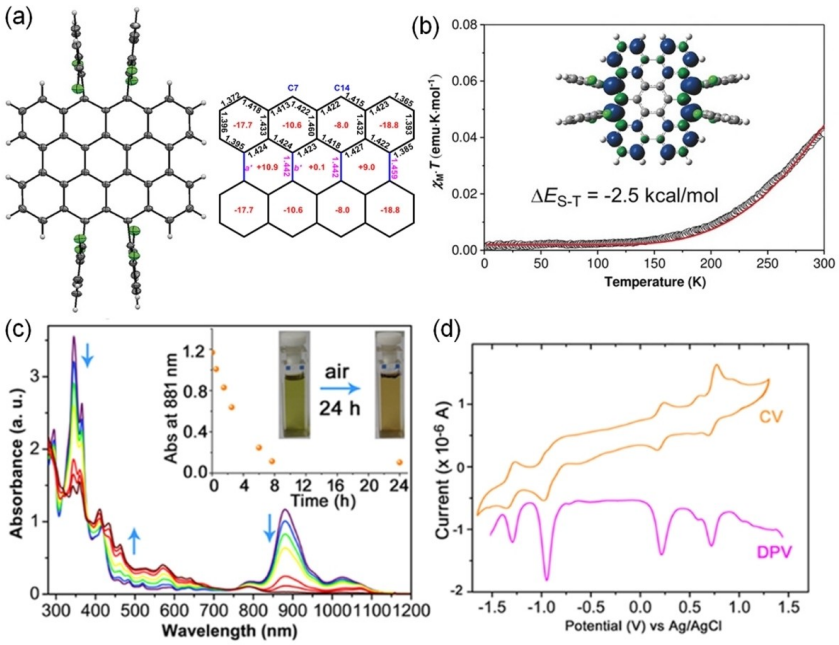

Figure 8. (a) X-ray crystallographic structure and selected bond lengths of the backbone of **25 b** (in Å). The red numbers in the hexagons are calculated NICS(1)$_{zz}$ values. (b) χ_MT–T plot in the SQUID measurement of the microcrystalline **25 b**. The solid line is the fitting curve according to the Bleaney–Bowers equation and inset is the calculated spin density distribution maps of the singlet diradical forms. (c) Time-dependent UV-vis-NIR absorption spectra of **25 a** under ambient conditions in CH_2Cl_2. (d) Cyclic voltammetry (CV) and differential pulse voltammetry (DPV) of **25 a** in a 0.1 M solution of $TBAPF_6$ in DCM. (a, b) Reproduced from Ref. [63] (c, d) Reproduced from Ref. [62] Copyright (2018), with permission from American Chemical Society.

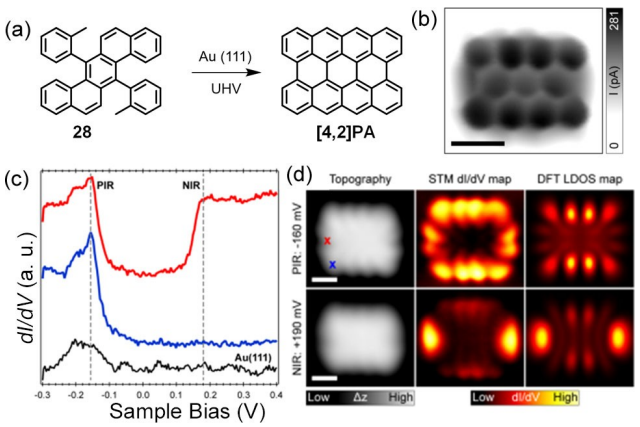

Figure 9. (a) On-surface synthesis of pristine [4,2]PA on Au(111). (b) Ultra high resolution STM image of [4,2]PA (scale bar = 0.5 nm). (c) d*I*/d*V* spectra on [4,2]PA (red and blue curves) acquired with a CO-functionalized tip. A reference spectrum on Au(111) is shown in black. The positions at which the spectra on the molecule were acquired are highlighted in the top-left image in (d) with red and blue crosses; (d) High-resolution STM images (left), simultaneously acquired d*I*/d*V* maps (center) and corresponding DFT-calculated LDOS maps (right) at the energetic positions corresponding to the PIR (top) and the NIR (bottom). Reproduced from Ref. [65] Copyright (2018), with permission from American Chemical Society.

13,13′-bis(dibromomethylene)-13*H*,13′*H*-6,6′-bipentacenylidene (**41**), and provided the in-depth electronic characterization of [5,2]PA on the Au(111) surface. Annealing **41** at 180 °C on Au(111) gave a minority of [5,2]PA as a side product coexisting with the formation of diradical one-dimensional [5.2]PA-based polymers. They have also performed the voltage dependant d*I*/d*V* spectroscopy for [5,2]PA on Au(111) with a CO functionalised STM tip (Figure 11f). The peaks obtained were assigned as HOMO-1, SOMO, SUMO and LUMO + 1, which was further supported with DFT simulation. The presence of an inelastic excitation was indicated by a stepwise change in conductance, which was ±40.5 meV around the Fermi energy. Together with the presence of singly occupied molecular orbitals, the inelastic excitation substantiated the occurrence of an antiferromagnetic singlet ground state.

Recently, Chi and co-workers[71] succeeded in the longitudinal extension of tetracene and reported the isolation of a stable [4,3]PA (tertetracene) derivative **48** in crystalline form. Similar to the aforementioned solution-based synthesis of [4,2]PA (Figure 7), a stable precursor (**47**) was synthesised by a four-step reaction strategy (Figure 12), which involved two-fold Suzuki coupling, ICl-mediated benzannulation, nucleophilic addition/Friedel-Crafts reaction and Scholl reaction. The dihydrogen precursor **47** was converted to the dianion by treating with KO^{t}Bu, which was in situ oxidized with *p*-chloranil to afford the final target compound **48** in 78% yield. The X-ray crystallography and the resultant bond length analysis (Figure 13a, Figure 13b) revealed the enhanced electronic coupling among the tetracene units of **48**, by observing short (a, b) bonds (Figure 13b). The NICS analysis (Figure 13b) inferred the possibility of eight localized Clar's sextets in the open-shell resonance structure of [4,3]PA. The natural orbital occupation number (NOON) analysis of [4,3]PA at UCAM-BLYP/6-31G(d,p) indicated the existence of a large degree of diradical character ($y_0 = 0.95$), which was higher than [4,2]PA ($y_0 = 0.72$). The

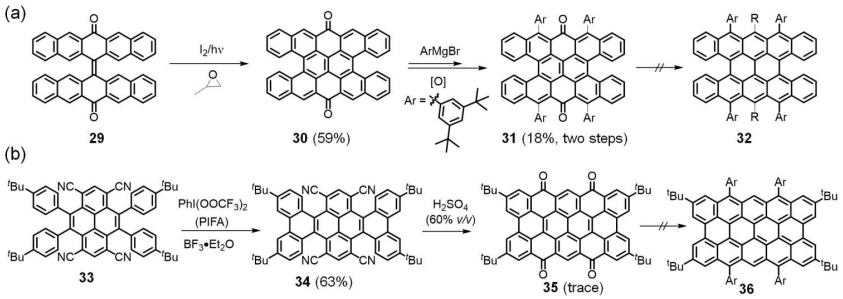

Figure 10. Attempted synthesis of *bis*-pentacene (a) and *peri*-pentacene (b).

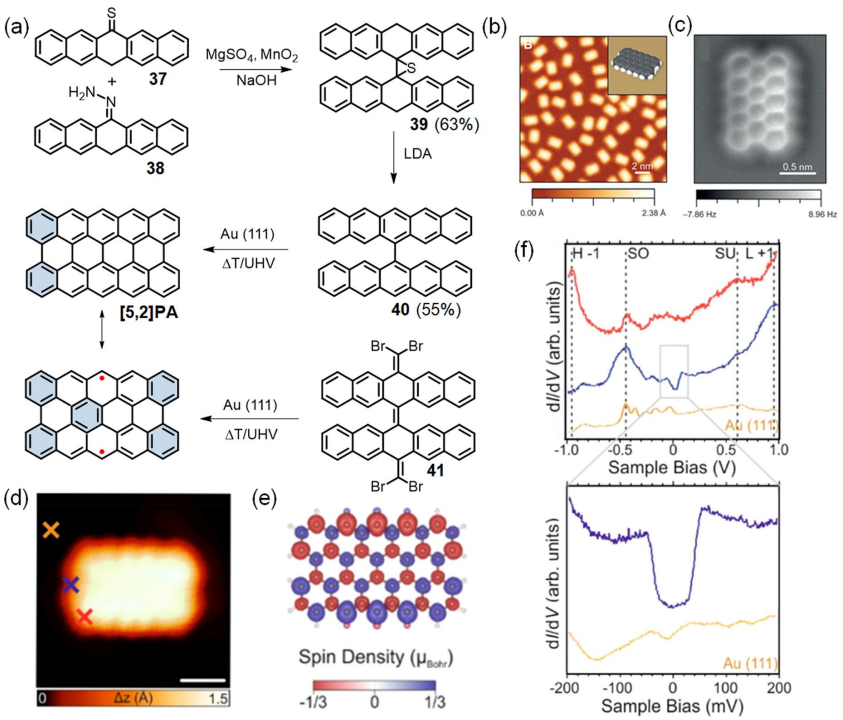

Figure 11. (a) Synthesis of [5,2]PA from two different precursors **40** and **41** on gold surface under UHV conditions. (b) Constant-current STM image of [5,2]PA on Au(111). (c) nc-AFM images of a single [5,2]PA on Au(111). (d) High-resolution STM topography image of a [5,2]PA. (e) Calculated spin density distribution of [5,2]PA using DFT–B3LYP. (f) Differential conductance spectra on selected positions of the [5,2]PA; the red and blue curves were acquired at the corner and apex positions of the molecule in (d). The orange curve corresponds to the reference d*I*/d*V* spectrum acquired on Au(111). (b, c) Reproduced from Ref. [69] (d–f) Reproduced from Ref. [70] Copyright (2020), with permission from American Chemical Society.

variable temperature EPR and SQUID measurements of **48**, fitted with Bleaney-Bowers equation, revealed a narrow $\Delta E_{S\text{-}T}$ gap (−0.57 kcal/mol from SQUID, Figure 13d). The high kinetic stability ($t_{1/2}$ = 157 h under ambient condition) could be attributed to the presence of electron-withdrawing zigzag substituents as well as the additional two *tert*-butyl groups at the corner. DFT based spin density analysis also proved that the zigzag C atoms with the phenyl substituents possessed the highest spin densities. The optical (Figure 13c) and electrochemical properties of [4,3]PA are comparable to [4,2]PA and the electrochemical ΔE_g was estimated to be 1.1 eV. Most likely, the larger diradical nature led to more localized aromatic feature, which increases the HOMO-LUMO gap and counterbalances the energy-gap decrease in [4,3]PA compared to [4,2]PA.

Encouraged by our earlier success in the synthesis of [4,2]PA in solution, we recently reported the in situ synthesis of [7,2]PA (namely, *peri*-heptacene) derivative **54**,[72] in which kinetic protection of the reactive zigzag edges were facilitated by incorporating eight *tert*-butyl phenyl groups. The synthesis of this highly persistent [7,2]PA was realised by using a fairly stable precursor **53**, which was synthesised by five-step reaction strategy (Figure 14). A one-pot iodine chloride-mediated benzannulation and intramolecular cyclodehydrogenation reaction of 4-(*tert*-butylphenyl)ethynyl functionalized oligophenylene (**51**) was the key step for this synthesis strategy. The obtained tetraiodo-scaffold **52** submitted for successive nucleophilic

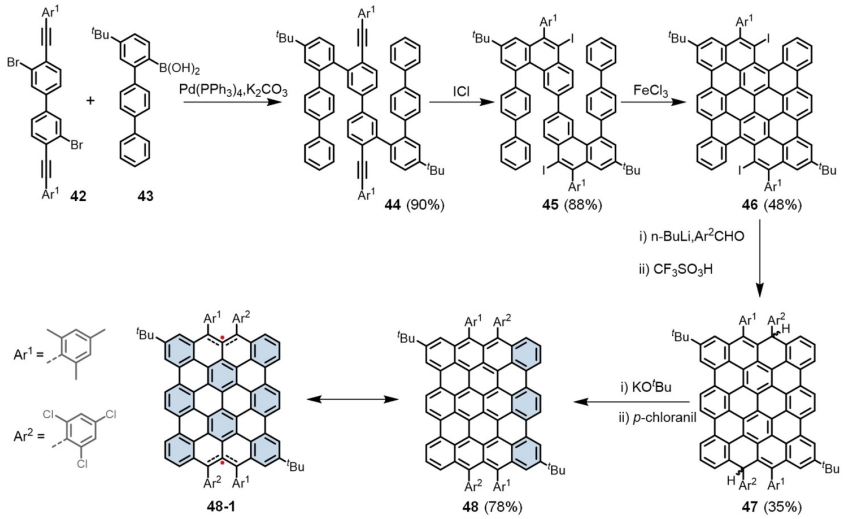

Figure 12. Synthesis of [4,3]PA **48**.

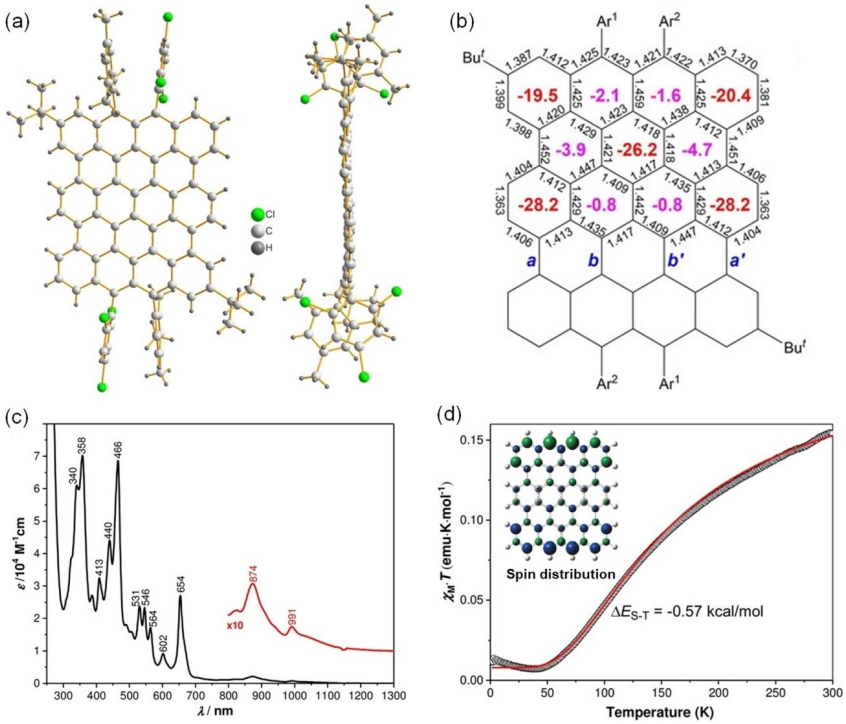

Figure 13. (a) X-ray crystallographic structures of [4,3]PA; (b) selected bond lengths of the backbone (in Å). The red/pink numbers in hexagons are the calculated NICS(1)zz values; the hexagons with large negative red numbers are correlated to aromatic sextets rings; (c) UV-Vis-NIR absorption spectra of [4,3]PA in DCM at room temperature; (d) $\chi_M T$–T plot in the SQUID of measurement of the [4,3]PA, the solid line (red) is the fitting curve according to Bleaney–Bowers equation. Inset is the spin density distribution map of singlet diradical form of parent [4,3]PA. Reproduced from Ref. [71].

addition and Friedel-Crafts reactions to afford the precursor **53** in 40% yield. The oxidative dehydrogenation of **53** with DDQ yielded the targeted **54** in situ, which was firstly supported by HR MALDI–TOF (Figure 15a) and EPR experiments. Towards the structural proof, in situ FT-Raman measurements (Figure 15b) were conducted and the obtained prominent G (1593 cm^{-1}) and D (1331 and 1402 cm^{-1}) bands were well supported by DFT simulations. The solution of **54** in toluene was persistently stable with a half-life time of 25 min and displayed clear vibronic structures, with an intense absorption peak centred at 812 nm along with four weak bands with maxima of 733, 924, 1050 and 1160 nm (Figure 15c). The optical bandgap was estimated to be 1.01 eV, which is lower than that of [4,2]PA and [4,3]PA. According to the occupation numbers of the lowest

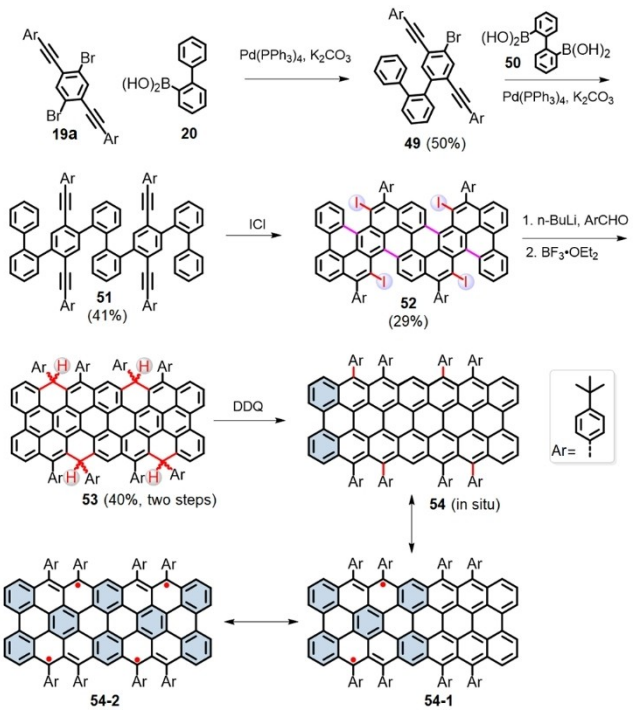

Figure 14. Synthesis of [7,2]PA **54**.

unoccupied natural orbitals (LUNO and LUNO + 1), the diradical character ($y_0 = 1.0$) and the tetraradical character ($y_1 = 0.22$) were calculated using CASSCF(8,8)/6-31G**, which are substantially higher than those of other reported PAs.

3. Heteroatom-Doped *peri*-Acenes

Heteroatom-doped PAs are interesting class of molecules that exhibit different optical, electronic and magnetic properties compared to their pristine hydrocarbon analogues.[73] The reactive zigzag edges of the PAs can be stabilised by the incorporation of heteroatoms (boron, nitrogen, or oxygen). However, the attractive open-shell properties associated with pristine PAs could not be preserved. Even though, the heteroatom doping is still a unique pathway to construct zigzag-edged NGs with appealing opto-electronic properties.

In 2015, a facile synthesis of a stable boron-containing bisanthene **59** was developed by Wagner and co-workers[74] based on Peterson olefination, photocyclization, and Si–B exchange reaction (Figure 16a). The single crystal characterization revealed that the compound **59** was largely planar with C_i-symmetry (Figure 16b). Notably, the B-doping transformed the near IR bisanthene dye into an efficient blue luminophore ($\Phi_{PL} = 78\,\%$), and thereby illustrated the impact of boron doping on the frontier orbitals of PAs (Figure 16c). The longest-wavelength absorption maxima (λ_{max}) of **59** were at 418, 432 and

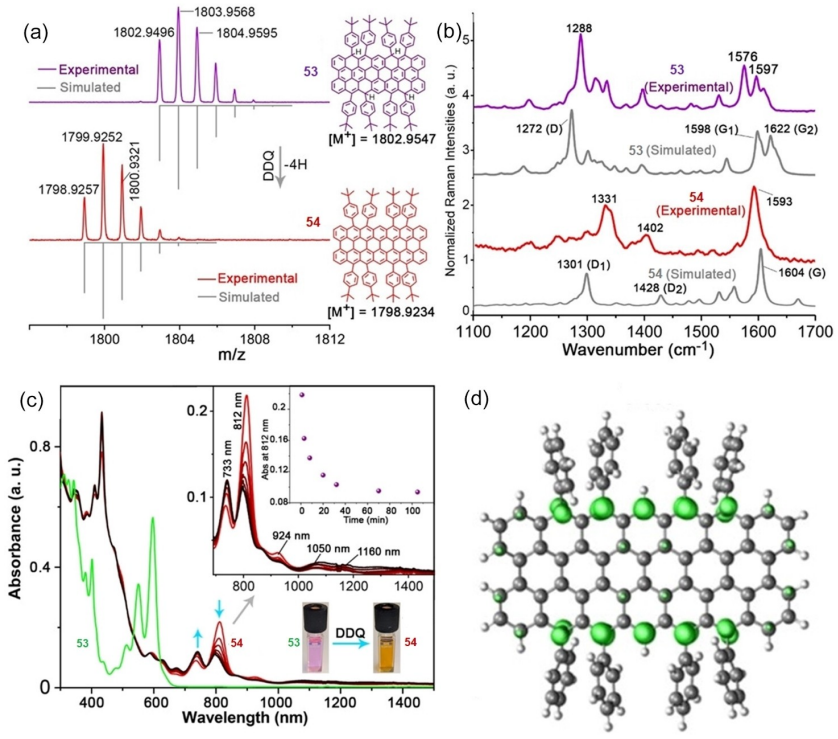

Figure 15. (a) HR MALDI-TOF mass spectra of **53** and **54**. The **54** was in situ generated by mixing toluene solution of **53** (8×10^{-4} M) with DDQ. (b) Experimental and simulated Raman spectra of precursor **53** and **54**. (c) UV-vis-NIR spectra of the tetrahydro-precursor **53** (green) (3×10^{-5} M) and the time-dependent absorption changes of the **54** (red) in dry toluene at RT under Ar (in the absence of light). The insets show the magnified view of NIR region and the absorbance (at 812 nm) of the **54** (under argon) at different time intervals. (d) Calculated (UCAM–B3LYP/6-311G**) density of the unpaired electrons of the singlet diradical form of [7,2]PA in gas-phase. Reproduced from Ref. [72].

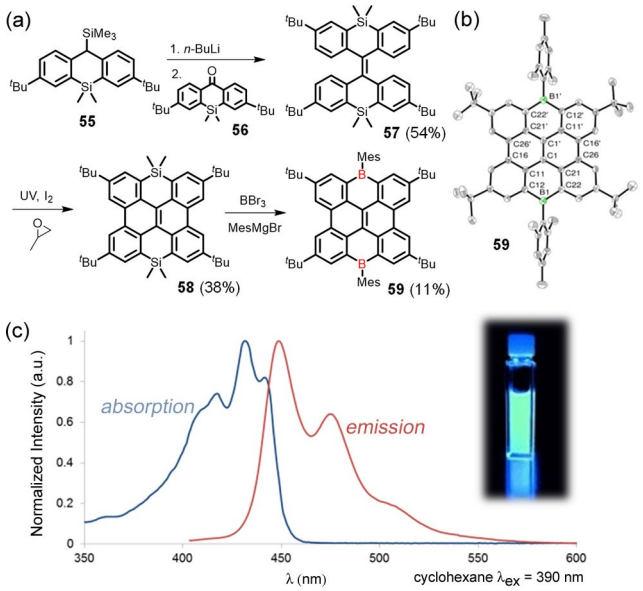

Figure 16. (a) Synthesis of B-doped bisanthene **59**. (b) Molecular structure of **59** in the solid state. (c) Normalized UV/Vis absorption and emission spectrum of **59** in cyclohexane. Inset: the solution under 365 nm UV light. Reproduced from Ref. [74].

442 nm, whereas the λ_{max} of the corresponding bisanthene derivative were at 625 and 685 nm. In addition, the optical energy gap for **59** (2.74 eV) was significantly larger than its bisanthene analogue (1.73 eV).

In 2016, we opened an opportunity to achieve PA-type NGs with stable zigzag edges by synthesising OBO-doped [4,2]PA **64**.[75] The precursor OBO-doped bistetracene **63** was synthesised by a tandem demethylation-aryl borylation strategy as shown in Figure 17a. The hexabromobenzene (**60**) was treated with (2-methoxyphenyl) magnesium bromide (**61**) to provide the 1,2,4,5-tetra(2-methoxyphenyl)benzene (**62**), which was later submitted for borylation in the presence of BBr_3 to get the OBO-doped bistetracene (**63 a** and **63 b**). The OBO-doped bistetracenes (**63 a** and **63 c**) were also obtained from a different method by Hatakeyama et al.,[76] where a diiodo-substituted intermediate **65** was used (Figure 17b). Finally, a cyclodehydrogenation reaction of the OBO-doped bistetracene (**63 a** and **63 b**) in presence of DDQ/TfOH yielded the planar derivatives **64 a** and **64 b** in high yield, respectively. The excellent stability of **63 b** facilitated further characterizations and the structure was confirmed by HR MALDI-TOF MS and ^{1}H NMR spectroscopy. Owing to the poor conjugation of O–B–O bonds, **64** exhibited a large HOMO-LUMO gap, and thereby high stability and significant fluorescence compared to its all carbon analogue [4,2]PA. The absorption and fluorescence spectroscopy of **64 b** (Figure 17c) presented well-resolved vibronic bands, which gave a blue fluorescence with a quantum yield of 27% and a narrow Stokes shift of 7 nm due to the rigid backbone structure. The comparison of NICS data of [4,2]PA and OBO-doped [4,2]PA (Figure 17d) implied that the heteroatoms significantly modified the electronic structures of the carbon framework. In addition, the energy gap of **64 b** (2.83 eV), estimated by the absorption spectroscopy, was higher than [4,2]PA (1.1 eV). Recently, NO-doped bistetracene (**68**) was synthesized and its optoelectronic properties were investigated.[77] Towards the synthesis, 12*H*-benzo[*b*]phenoxazine (**66**) was treated with DDQ and the obtained cruciform dimer **67** was converted into **68** in 69% yield in the presence of DDQ and $Sc(OTf)_3$ (Figure 17e). The molecular structure of **68** was unambiguously confirmed by X-

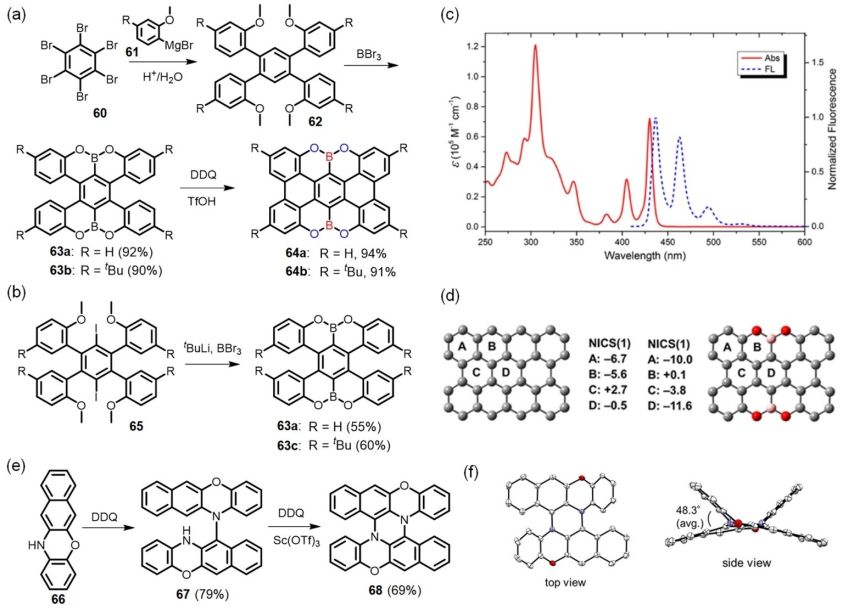

Figure 17. (a) Synthesis of OBO-doped [4,2]PA **64**. (b) Another method to synthesize the uncyclized precursors **63 a** and **63 c**. (c) Absorption and fluorescence spectra of **64 b** in CH_2Cl_2 (1×10^{-5} M). (d) DFT-calculated NICS(1) values (in ppm) of [4,2]PA (left) and OBO-doped [4,2]PA (right). (e) Synthesis of NO-doped bistetracene **68**. (f) Molecular structure of **68** in the solid state. (c and d) Reproduced from Ref. [75] Copyright (2016), with permission from American Chemical Society. (f) Reproduced from Ref. [77] Copyright (2021), with permission from American Chemical Society.

ray crystallography (Figure 17f). Compared to the all-carbon analogue **12**, the NO-doped bistetracene **68** was non-magnetic and characterized with a larger energy gap, i.e., 3.18 eV.

Later, this strategy was further extended for the on-surface synthesis of OBO-doped [6,2]PA **72** by us.[78] As shown in Figure 18a, the hexabromobenzene **60** was firstly treated with respective methoxy-naphthalene based Grignard reagent **69** and quenched with iodine. The obtained intermediate **70** was lithiated and then borylated in presence of BBr_3 to provide the double helicene precursor **71** in a yield of 43%. However, oxidative cyclodehydrogenation reaction of **71** in solution did not yield the planarized product and gave mixtures of undefined products. With the assistance of on-surface cyclodehydrogenation, the precursor **71** was converted into planar OBO-doped **72** on the Au(111) surface and the *peri*-hexacene skeleton of the targeted molecule was visualized by STM and nc-AFM (Figure 18b,c). Furthermore, **72** formed two kinds of 1D superstructures (Figure 18d) through intermolecular hydrogen bonding and metal coordination with the OBO segments on the zigzag edges. Additionally, X-ray photoelectron spectroscopy and Raman spectroscopy combined with DFT studies also further supported the formation of **72**.

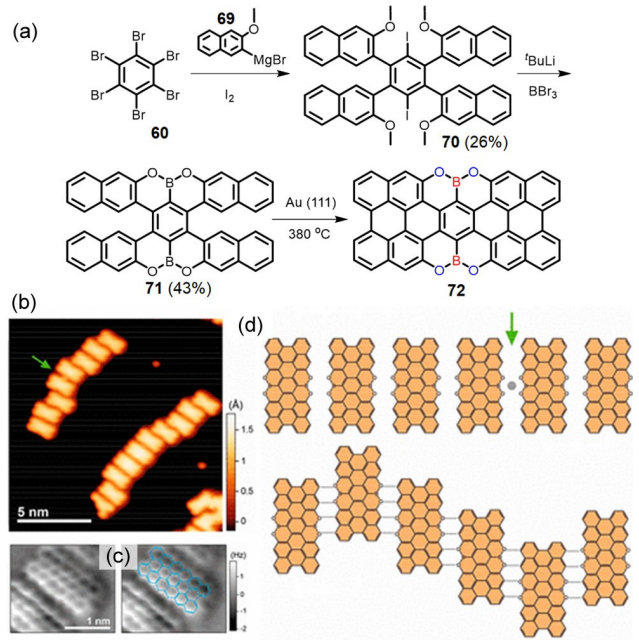

Figure 18. (a) Synthetic route to OBO-doped [6,2]PA **72**. (b) STM and (c) CO-sensitized nc-AFM images of **72**. Reproduced from Ref. [78] Copyright (2017), with permission from American Chemical Society.

Although the OBO-doping stabilises the zigzag-edges of PAs, it significantly diminishes the electronic conjugation and quenches the attractive open-shell properties of the all-carbon analogues. Therefore, we turned to the synthesis of NBN-doped PAs, which is more fascinating due to the possibility of isosterism.[79,80] In this regard, we recently accomplished a stable NBN-doped [4,2]PA **81** by combining the solution-based and surface-assisted synthesis (Figure 19).[81] The NBN-doped bistetracene precursor **80** was synthesised via a tandem two-fold electrophilic borylation approach based on a tetra(aminophenyl)-benzene molecule **79** in 20% yield. The targeted compound **81** was then achieved from the precursor **80** through solution-based photocyclization or by surface-catalysed cyclodehydrogenation reaction on Au (111) as shown in the Figure 19a. The formation of the **81** was confirmed by STM and nc-AFM (Figure 19b,c). The HOMO and LUMO energy levels of **81** were estimated to be −0.88 eV and 2.40 eV on Au(111) based on the STS characterisation (Figure 17d). The corresponding energy gap of **81** (3.28 eV) was significantly higher than that of pristine all-carbon [4,2]PA on Au(111) (0.35 eV). Moreover, the isosterism phenomenon of the oxidized **81** with [4,2]PA was also demonstrated by DFT calculations. The energy gaps of the doubly oxidized **81**, i.e., $\mathbf{81}^{2+}$ ($\Delta E_g = 1.21$ eV) was calculated to be significantly lower than neutral **81** (3.37 eV), whereas comparable to [4,2]PA (1.76 eV), and thereby revealed their isoelectronic relationship.

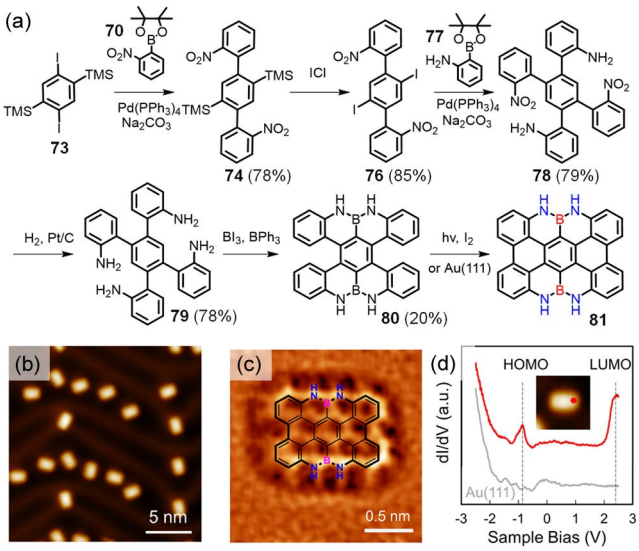

Figure 19. (a) Synthesis of NBN-doped [4,2]PA **81** via solution-phase and on-surface methods; (b) STM topography image of **81**; (c) nc-AFM image of **81** on Au(111); (d) d*I*/d*V* spectrum of **81** (red) and Au(111) (grey). Scanning parameters: (a, b) $V_s = -1$ V, $I_t = 50$ pA; (d) amplitude = 100 pm; $V_s = -2.5$ V, $I_t = 800$ pA, $V_{mod} = 20$ mV. Reproduced from Ref. [81].

4. PA-Based Graphene Nanoribbons and PA-Bridged Cumulene Polymers

Apart from the relatively small PA motifs, their π-extended structures, i.e. zigzag-terminated armchair GNRs (AGNRs), ZGNRs and chiral GNRs, are also highly interesting, especially in view of the future development of carbon-based spintronics and quantum devices (Figure 20).[82–83] The AGNRs are usually represented as N-AGNRs based on their width, where N is the width indicated by the number of rows of C atoms across the AGNRs. The bottom-up and syntheses of AGNRs via on-surface and solution-phase strategy are highly feasible. Moreover, the bandgaps of the AGNRs can be tuned by changing the width as well as with the incorporation of various heteroatoms (vide

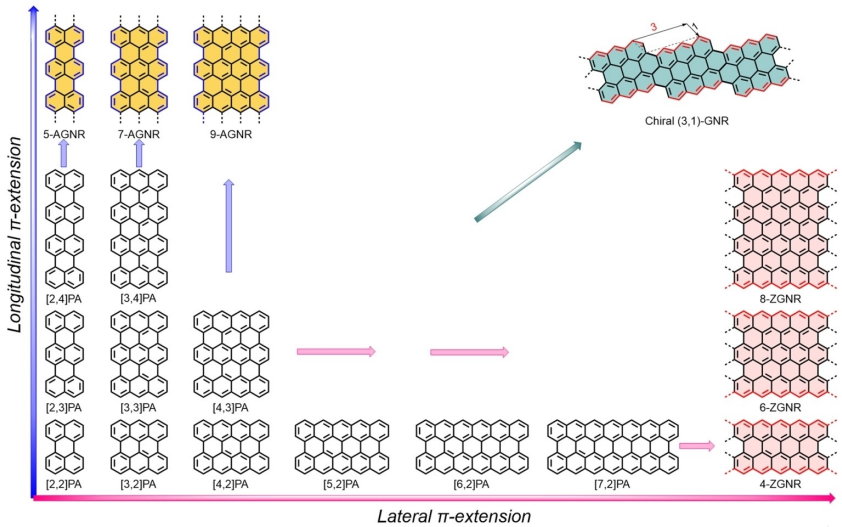

Figure 20. Extension of perylene ([2,2]PA) along lateral and longitudinal dimensions leading to a variety of π-extended PAs, AGNRs, ZGNR and chiral GNRs.

infra). However, the solution-based synthesis of PA-based AGNRs (Figure 20) with zigzag terminus was not reported so far. In 2010, our group in collaboration with Müllen and Fasel et al.[84] firstly demonstrated the on-surface synthesis of 7-AGNR (**84**) with zigzag termini under UHV conditions from the 10,10′-dibromo-9,9′-bianthryl (**82**) (Figure 21a). Upon annealing, the precursor **82** underwent metal-surface-assisted Ullmann homo-coupling on Au (111) to form the polymer **83**, which was transformed to **84** after surface-assisted cyclodehydrogenation at elevated temperature (400 °C). We have performed local

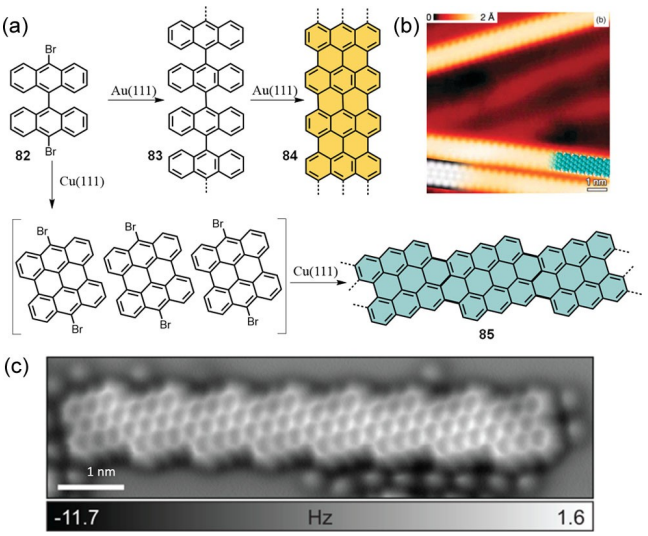

Figure 21. (a) On-surface synthesis of 7-AGNR (**84**) on Au(111) and chiral (3,1)-GNR (**85**) on Cu(111) from dihaloginated bianthryl monomer **82**, respectively. (b) High-resolution STM image with partly overlaid molecular model (blue) of the ribbon. At the bottom left is a DFT-based STM simulation of the 7-AGNR shown as a greyscale image. (c) nc-AFM image of the chiral (3,1)-GNR (**85**) on Cu(111). (b) Reproduced from Ref. [85] Copyright (2012), with permission from American Chemical Society. (c) Reproduced from Ref. [86] Copyright (2014), with permission from American Chemical Society.

electronic characterization of **84** using STM STS (Figure 21b). A bandgap of 2.3 eV was estimated for the 7-AGNR **84** with the aid of angle-resolved photoelectron spectroscopy and STS on Au(111).[85] Interestingly, in 2014, Han and Asao et al.[86] reported that the same monomer **82** undergoes intermolecular cyclodehydrogenation at different configurations on a Cu(111) surface, leading to an unprecedented formation of bisanthene-based chiral-edge (3,1)-GNR **82** (Figure 21a). Later on, the formation of chiral (3,1)-GNR **82** on Cu(111) was clearly revealed with the help of nc-AFM with CO-functionalized tips.[87] Actually, the (3,1)-GNR **85** were obtained from the halogen-free sister molecule 9,9′-bianthryl, proving that halogen functionalization plays no role in this system. Under oxidizing environments, the zigzag edges of **85** were vulnerable to oxidation and the electronic properties did not survive.[88] However, it was also proved that the oxidized **85** on Au(111) could be transformed to the pristine form upon hydrogenation and annealing under UHV condition.[89]

Very recently, Pascual et al.[90] synthesized a series of chiral GNRs **85, 88, 90** and **92** on Au(111) with different chirality and widths, by using various predesigned dibrominated anthracene-based precursors **86, 87, 89** and **91** (Figure 22a–d). As shown in Figure 22e–h, the structure of GNRs **85, 88, 90** and **92** were clearly revealed by STM measurements. By using these chiral GNRs, they evaluated the relationship of topological states with width, length, and chirality. The wider chiral GNRs (**88** and **90**) exhibited a characteristic current increase over the edges, which was absent in the GNRs **85**. This provided an experimental evidence for the emergence of edge bands in the wider ribbons. Interestingly, GNRs **92** revealed zero-energy topological modes at the termini. The respective d*I*/d*V* spectra of **92** demonstrated a sharp peak at zero bias for the terminal zigzag position, whereas a 300 meV bandgap was found for the zigzag periphery at bulk region.

On the other hand, the heteroatom doping (B, O, N, etc.) into the carbon framework of GNRs has also significant

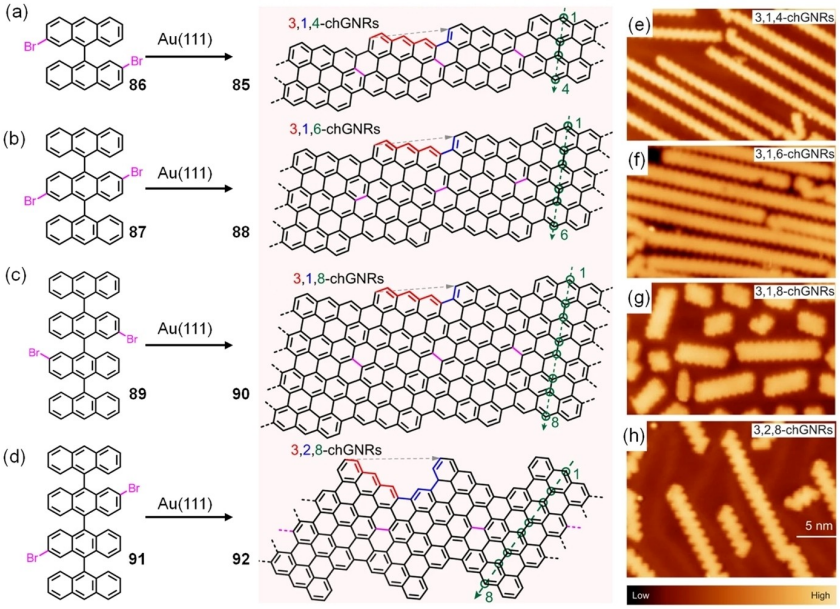

Figure 22. (a-d) The chemical structures of chiral GNRs (**85**, **88**, **90** and **92**) by using the four molecular precursors (**86**, **87**, **89** and **91**), respectively. (e-h) STM overview images of the chiral GNRs formed on a Au(111) surface after stepwise annealing the sample covered with respective precursors. Reproduced from Ref. [90] Copyright (2021), with permission from Springer Nature.

interest.[91–93] Considering the electron deficiency and Lewis acidity, B is a unique element and its incorporation into aromatic carbon framework of GNRs offers a wide variety of functionality.[94,95] However, the synthesis of such boron-doped graphene nanoribbon was hampered due to the intrinsic instability of suitable organoboron precursors[96] under ambient conditions. In 2015, the synthesis of the first boron-doped graphene nanoribbon (B-GNRs) was independently accomplished on Au (111) by Fischer's group[97] and by Kawai et al.[98] (Figure 23a) from an organoboron precursor **93**, namely 9,10-bis(10-bromoanthracen-9-yl)-9,10-dihydro-9,10-diboraanthracene. The precursor **93** on Au (111) underwent dehalogenation at 180 °C under UHV and thereby triggered the linear polymerisation. Finally, the surface-assisted cyclodehydrogenation of the polymer **94** occurred at 400 °C and resulted in the formation of B-doped 7-AGNRs **95**. The structure and the electronic properties of B-GNRs **95** were elucidated by STM, high-resolution nc-AFM and DFT computations (Figure 23b–d). The d*I*/d*V* studies were conducted for **95** and the bandgap was estimated to be 2.4 eV, which was comparable to the non-doped GNR (**84**) on Au(111). In **95**, the B atoms were located at the centre and could not provide any significant electron-hole asymmetry. Therefore, B-doping in **95** did not influence the overall electronic structure. In addition, it was also observed that the armchair edges of the B-doped 7-AGNRs **95** could fuse at high temperature (500 °C) and led to the formation of B-doped 14-AGNRs and 21-AGNRs. In 2020, the evolution of a magnetic ground state was achieved by inserting a pair of B atoms in the 7-AGNRs by Pascual and co-workers (Figure 23f).[99] Towards the synthesis, the bisanthene precursor **82** along with a small portion B-doped molecule **93** were evaporated and allowed for the surface-assisted polymerisation and cyclodehydrogenation. The structure of the resultant GNR **96** were confirmed by STM analysis (Figure 23g). The doping of a pair of B atoms broke the conjugation of their topological bands and consequently two spin-polarized boundary states around them were generated. The spin state was detected in electrical transport measurements through the 2B-7-AGNR **96** suspended between a tip and sample.

Moreover, Kawai et al. also successfully synthesized a pair of isomers of B/N-doped 7-AGNRs (**99** and **102**), by using 5-(10-chloroanthracen-9-yl)-10-(10-iodoanthracen-9-yl)-5,10-dihydrodibenzo[*b*,*e*][1,4]azaborinine (**97**) precursor (Figure 24).[100] Due to the asymmetric structure, the precursor **97** induced polymerisation via I–Cl and I–I coupling and led to isomers of B/N-doped GNRs **99** and **102**. Based on the STM investigation, it was found that the resultant B/N-doped GNRs were shorter than the pristine 7-AGNR (**84**) as well as B-doped GNR **95**. The dark triangular feature was more pronounced in the nc-AFM images that implied the presence of only one B at the centre of the doped anthracene moiety. Similar to the case of **95**, the B/N atoms were placed on the center of **99** and **102** did not influence significantly the overall electronic properties of the GNR. Therefore, the bandgaps of **99** and **102** (2.3 eV) were comparable to that of **84** (2.3 eV) and **95** (2.4 eV).

Unlike the AGNRs, the ZGNRs comprise zero bandgaps and can demonstrate unique half-metallic and magnetic properties due to the presence of the spin polarised the edge-states. Due to the poor chemical stability, the syntheses of ZGNRs have been limited thus far to on-surface synthesis under UHV conditions. In 2016, Fasel, Müllen, and us realised the first bottom-up synthesis of a fully zigzag-edged GNR (6-ZGNR) **108** on Au(111) surface (Figure 25a).[39] In this protocol, a rationally synthesised U-shaped dibenzoanthracene-based precursor **106**

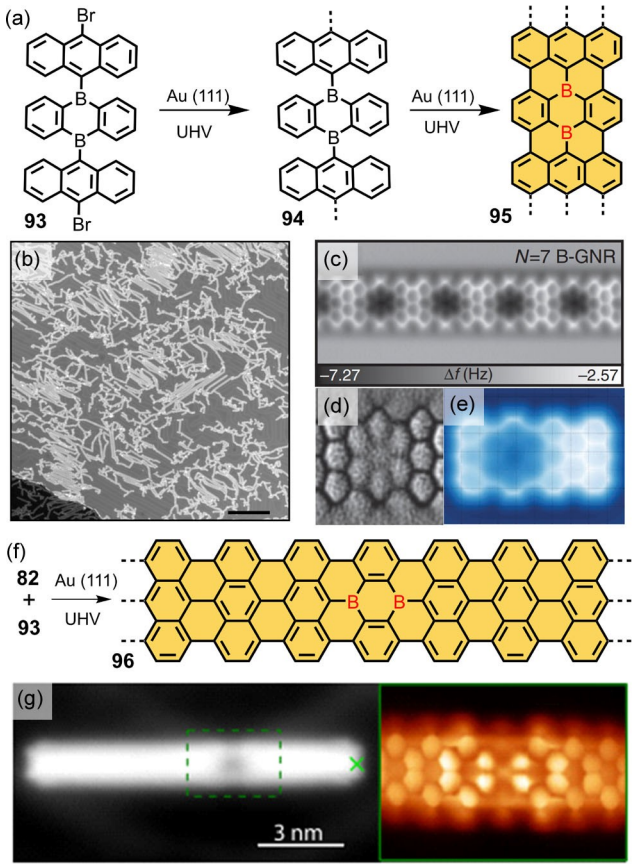

Figure 23. (a) Schematic drawing of the on-surface synthesis of B-doped 7-AGNRs (**95**). (b) STM overview showing the formation of **95** by annealing at 400 °C (scale bar = 30 nm). (c) nc-AFM image of single **95** taken using a CO-functionalized tip. (d) The Laplace filtered image and (e) the simulated AFM image of **95**. (f) Scheme illustrates the synthesis of a 2B-atom doped 7-AGNR **96** on Au(111) under UHV condition. (g) STM constant current topography image and constant height current scan using a CO-functionalized tip of **96**. (b–e) Reproduced from Ref. [98] Copyright (2015), with permission from Springer Nature. (g) Reproduced from Ref. [99] Copyright (2020), with permission from American Physical Society.

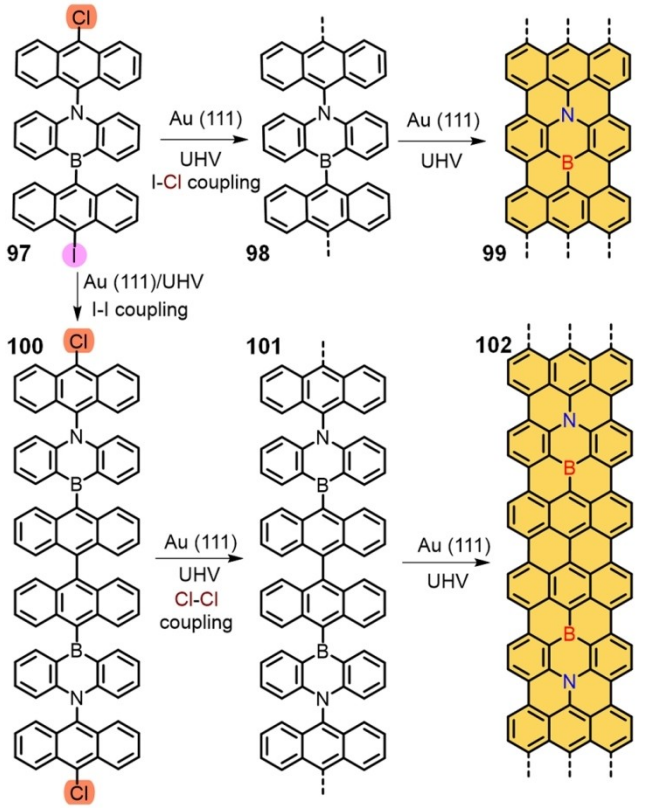

Figure 24. Schematic drawing of the on-surface synthesis of long- and short-periodicity B/N-doped 7-AGNRs **99** and **102**.

with two halogen functions was submitted for thermally induced surface-assisted polymerization at 200 °C in order to form a snake-type polymer **107**. Upon the subsequent cyclodehydrogenation at 350 °C, the two preinstalled methyl groups of the polymer **107** bridged with the neighbouring phenyl rings and rendered a fully zigzag-edged GNR **108**. The formation of **108** on Au(III) was directly observed by STM and nc-AFM techniques (Figure 25b, Figure 25c). The nc-AFM imaging with a CO-functionalized tip confirmed that the observed width and edge morphology corresponded to the expected ribbon structure. The small bandgap (1.5 eV) and the high electron density localized on the zigzag edges of the 6-ZGNR **108** was revealed by the analyses of the local density of state (DOS) and the d*I*/d*V* spectra of **108** observed on NaCl plates (Figure 25d). These observed features in comparison with the simulated DOS maps, evidenced the existence of the unperturbed zigzag edge states. The respective experimental and DFT simulated d*I*/d*V* maps also support the presence of highly localized zigzag edge states (Figure 25e, Figure 25f).

Very recently, a N-doped 6-ZGNR **115** (N-6-ZGNR) was synthesized on-surface by Fischer and co-workers,[101] where every sixth C–H group along the zigzag edge of a 6-ZGNR was replaced by a N atom (Figure 26). Similar to the synthesis of 6-ZGNR **108**, a suitable U-shaped monomer **113** bearing one N atom on the zigzag edge (Figure 26a) was synthesized starting from 7-bromonaphthalen-2-ol (**109**) via two steps and sublimed in ultrahigh vacuum (UHV) onto a clean Au(111) surface (Figure 26b). Annealing at 475 K induced the polymerization of the monomer, and further annealing at 650 K caused the thermal cyclodehydrogenation that provided the fully fused **115**. STM topographic images revealed the extended ribbons **115** featuring atomically smooth zigzag edges (Figure 26c-e). The d*I*/d*V* spectroscopy (Figure 26f) was performed to examine the local electronic structure of the surface-decoupled **115** and the bandgap was estimated to be $\Delta E_g = 0.80 \pm 0.05$ eV, which was significantly lower than that of the pristine all-carbon 6-ZGNR **108**. Furthermore, a giant spin splitting of low-lying nitrogen lone-pair flat bands induced by the ferromagnetically ordered spins along the edge of **115** was also experimentally observed.

The PAs can also bridge with ethynylene groups in order to build narrow-bandgap π-conjugated polymer wires. In 2020, Ecija et al.[102] accomplished bisanthene polymer wires on Au(111) surface (Figure 27a) using 10,10′-bis(dibromomethylene)-10*H*,10′*H*-9,9′-bianthracenylidene precursor (**116**). The

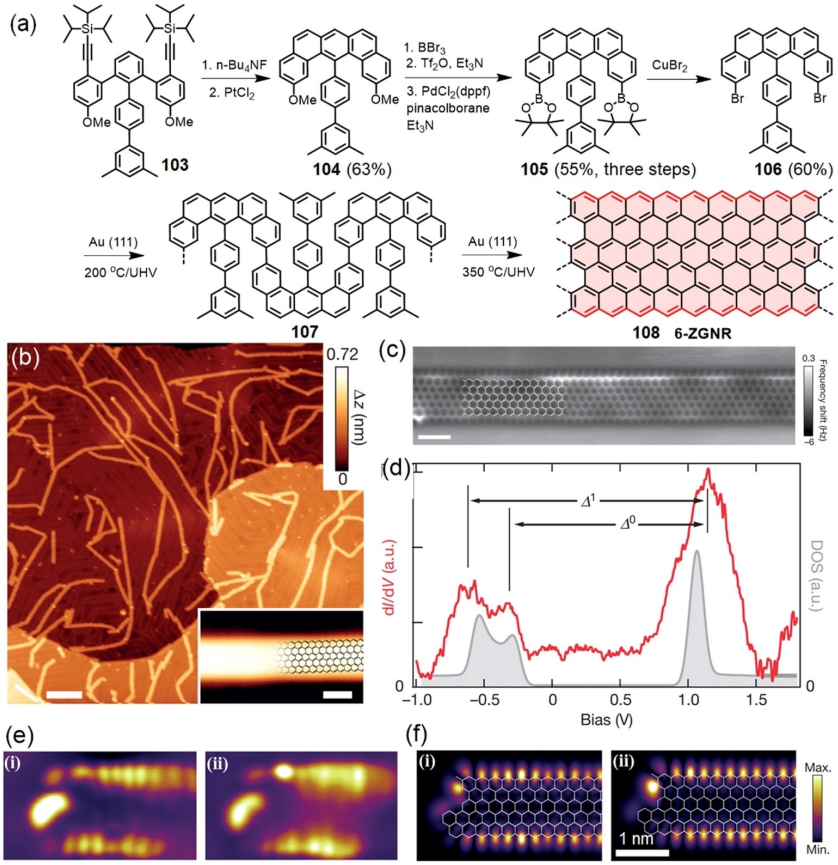

Figure 25. (a) The synthetic route towards the U-shaped monomer **106** with two preinstalled methyl groups and its on-surface reaction for realising 6-ZGNR **108** on Au (111). (b) STM image of **108** on Au(111) surface (Scale bar = 20 nm). Inset, high-resolution STM of a **108** (Scale bar = 1 nm). (c) The nc-AFM image of **108** taken with a CO-functionalized tip (Scale bar = 1 nm). (d) d*I*/d*V* spectrum (red) taken at the zigzag edge and the quasiparticle density of states (DOS; grey). (e) d*I*/d*V* maps of filled (i) and empty (ii) edge states taken at a sample bias of −0.3 V and 1.0 V, respectively. f) DFT-based local DOS at a 4-Å tip-sample distance, showing the spatial distribution of filled (i) and empty (ii) edge states. Reproduced from Ref. [39] Copyright (2016), with permission from Springer Nature.

molecular structure of the wire **117** was visualised using nc-AFM imaging with a CO tip, where the planar and bisanthene moieties were linked by linear ethynylene (cumulene) bridges (Figure 27b, Figure 27c). Interestingly, the edge states resulting from the non-trivial topological character of the wire can also be observed in large-scale constant-height nc-AFM and STM images. The bulk electronic structure of the wire was examined with DFT and STS analysis and found both are in excellent agreement (Figure 27d–f). The two peaks at −75 meV and 200 meV in the d*I*/d*V* plot were corroborated to the edge of valance band (VB) and conductance band (CB) and the bandgap was estimated to be ~0.3 eV. Also obtained very good matching between the experimental and simulated d*I*/d*V* maps of the VB and CB edges. Upon further annealing at 650 K, the **117** wire underwent two-fold cyclization reaction between adjacent bisanthene moieties and obtained a long pentalene-bridged conjugated ladder polymer.[103] In 2020, they further extended this chemistry to build one-dimensional cumulene-like polymers **118** based on [5,2]PA units.[104] Towards the synthesis of **118**, on-surface reactions of 13,13′-bis(dibromomethylene)-13*H*,13′*H*-6,6′-bipentacenylidene precursor (**41**) was performed on Au(111) under UHV conditions (Figure 27g). The structural characterisation of the polymer wire **118** was provided by means of high resolution STM and nc-AFM imaging (Figure 27i, Figure 27j). STS analysis combined with theoretical calculations unravelled its electronic and magnetic properties (Figure 27k). The polymer wire **118** exhibited a narrow ΔE_g of ~0.8 eV and monoradical states at each terminus (Figure 27h).

5. Conclusions and Perspectives

We have summarized the recent progress on the design, synthesis, characterization, and properties of PAs and their π-extended analogues. The synthesis of larger [n,m]PAs beyond a certain [n,m] value is challenging as a result of their inherent open-shell radical characters. Although the bisanthene ([3,2]PA) was synthesised in 1948, its larger open-shell analogue [4,2]PA was recently reported by our group from both solution-phase and on-surface syntheses. However, the synthesis of [5,2]PA was not yet reported in solution, whereas it was only successfully realised on Au(111) under UHV conditions. Very recently, the longest [7,2]PA reported to date with significant tetradical

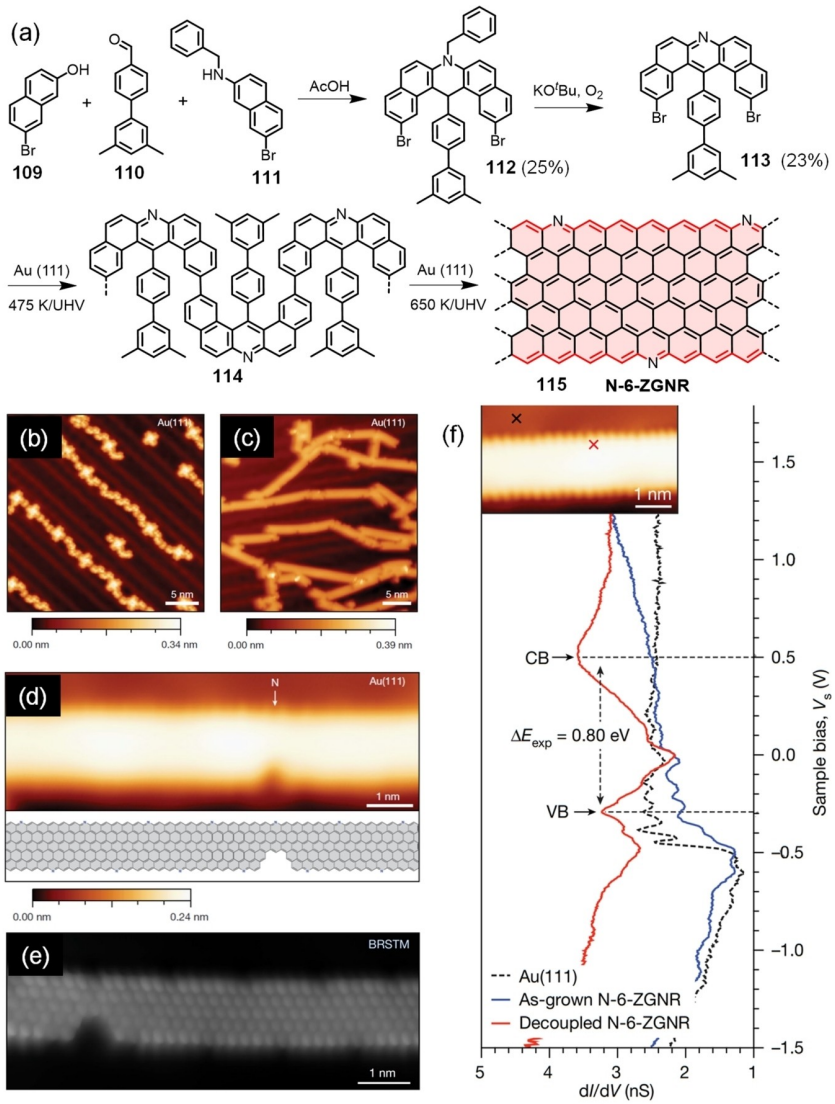

Figure 26. (a) Schematic representation of the on-surface synthesis of N-6-ZGNR (**115**) from molecular precursor **113**. (b) STM topographic image of molecular precursor **113** as deposited on Au(111). (c) STM topographic image of fully cyclized **115**. (d) STM image of **115** featuring a single point defect resulting from the cleavage of an m-xylene group. (e) Bond-resolved STM image of **115** segment following tip-induced decoupling using a negative voltage sweep from $V_s = 0.0$ V to -2.5 V. (f) dI/dV point spectroscopy of **115**/Au(111). Reproduced from Ref. [101] Copyright (2021), with permission from Springer Nature.

character ($y_1 = 0.22$) was synthesised and characterised by us, where eight phenyl groups were provided to protect the zigzag peripheries. Instead of the lateral extension of [4,2]PA, the longitudinal extended tertetracene ([4,3]PA) was successfully synthesized and isolated in solution, which shown a larger degree of diradical character ($y_0 = 0.95$) than the [4,2]PA ($y_0 = 0.72$).

As an alternative strategy, the introduction of heteroatoms on the zigzag edges of PAs was emerged as a powerful method to stabilize the pristine PAs and tune their optical, electronic, and magnetic properties. Such properties are largely dependent not only on the heteroatom type (i.e., boron, oxygen, nitrogen) but also on the doping position and concentration. In recent years, various heteroatom-doped PAs were synthesized by both solution-phase and on-surface methods, including the boron, OBO and NBN incorporation. The OBO-doping could enhance the stability of PAs, but it significantly diminishes the electronic conjugation and quenches the open-shell character of the all-carbon analogue. However, NBN-doping on the zigzag edges of PAs can mimic the electronic property of their open-shell all-carbon analogue after further oxidation or reduction in view of the BN/CC isosterism. For example, the NBN-doped [4,2]PA that was synthesized by us exhibited excellent stability and its dication possessed a similar energy gap with the unstable all-carbon [4,2]PA, indicating their isoelectronic relation.

Moreover, PAs can serve as model compounds for GNRs to reveal the length dependent properties. However, such exotic PA-based GNRs and polymers are inaccessible in wet-chemistry due to the high intrinsic reactivity, whereas on-surface method provides the opportunity not only to visualise but also to explore the magnetic and electronic properties of such π-extended analogues. For example, the PA-based zigzag-termi-

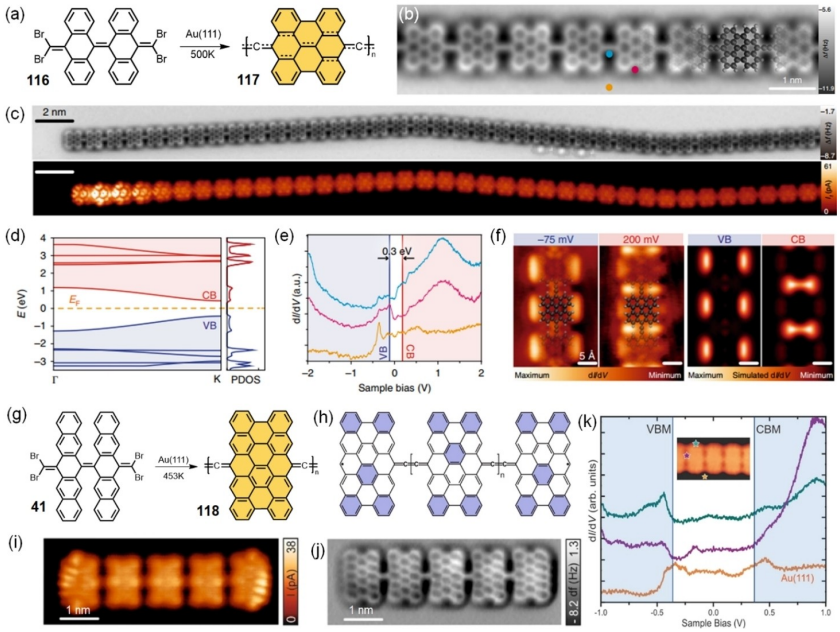

Figure 27. (a) Reaction pathway for the on-surface synthesis the [3,2]PA-based cumulene polymer wire **117** on Au(111). (b) nc-AFM image of **117** with the superimposed model. (c) Large-scale constant-height nc-AFM and STM images of **117**. (d) Calculated band structure and projected DOS (PDOS). (e) Experimental determination of ΔE_g with STS at the positions depicted by coloured dots in b. (f) Constant current d*I*/d*V* maps of the VB and CB (left) with the corresponding simulated maps (right). (g) The on-surface synthetic scheme towards the synthesis of cumulene-bridged [5,2]PA polymer wire **118** and its (f) open-shell non-Kekulé structure. (i) Constant-height ultrahigh-resolution STM image of **118** acquired with a CO-functionalized tip showing LDOS at each longitudinal polymer edge. (j) Constant-height frequency-shift nc-AFM image of **118** acquired with a CO-functionalized tip. (k) d*I*/d*V* spectra acquired on a decamer (purple and green curves) at the positions marked with purple and green stars respectively in the inset STM image. (b–f) Reproduced from Ref. [102] Copyright (2020), with permission from Springer Nature. (h–k) Reproduced from Ref. [104].

nated AGNRs and chiral GNRs as well as the PA-bridged polymers bearing linear cumulene chains were realized on surface. Notably, the first atomically precise 6-ZGNR was also synthesized on an Au (111) substrate based on a predesigned U-shaped monomer. Similar to the heteroatom-doped PAs, the heteroatom doping also opened up new avenues here to fine-tune the electronic structure of PA-based GNRs, even inducing a spin polarised state in B-doped 7-AGNRs.

Overall, last decade has witnessed some remarkable advancement in the synthesis and characterization of PAs, but still only a handful of them were realised in solution chemistry due to their intrinsic reactivity, especially for the synthesis of π-extended PA-based GNRs. To move forward from the infancy stage of this topic, the synthetic chemists need to firstly circumvent the poor stability of π-extended PAs by rational synthetic strategy, and close collaborations with physicists and material scientists are also required to push their applications not only in nanoelectronics, but also in the emerging carbon-based spintronics.

Acknowledgements

This research was financially supported by the EU Graphene Flagship (Graphene Core 3, 881603), ERC Consolidator Grant (T2DCP, 819698), H2020-EU.1.2.2.– FET Proactive Grant (LIGHT-CAP, 101017821), the Center for Advancing Electronics Dresden (cfaed) and DFG-NSFC Joint Sino-German Research Project (EnhanceNano, No. 391979941), as well as the DFG-SNSF Joint Switzerland-German Research Project (EnhanTopo, No. 429265950). Open Access funding enabled and organized by Projekt DEAL.

Conflict of Interest

The authors declare no conflict of interest.

Keywords: *peri*-Acenes · Graphene nanoribbons · Heterocycles · Nanographenes · Radicals

[1] J. Wu, W. Pisula, K. Müllen, *Chem. Rev.* **2007**, *107*, 718–747.
[2] A. Narita, X.-Y. Wang, X. Feng, K. Müllen, *Chem. Soc. Rev.* **2015**, *44*, 6616–6643.
[3] W. Xu, T.-W. Lee, *Mater. Horiz.* **2016**, *3*, 186–207.
[4] X. Li, X. Wang, L. Zhang, S. Lee, H. Dai, *Science* **2008**, *319*, 1229–1232.
[5] L. Chen, Y. Hernandez, X. Feng, K. Müllen, *Angew. Chem. Int. Ed.* **2012**, *51*, 7640–7654; *Angew. Chem.* **2012**, *124*, 7758–7773.
[6] K. Nakada, M. Fujita, G. Dresselhaus, M. S. Dresselhaus, *Phys. Rev. B* **1996**, *54*, 17954.
[7] Y.-W. Son, M. L. Cohen, S. G. Louie, *Phys. Rev. Lett.* **2006**, *97*, 216803.
[8] H. Nagai, M. Nakano, K. Yoneda, H. Fukui, T. Minami, S. Bonness, R. Kishi, H. Takahashi, T. Kubo, K. Kamada, K. Ohta, B. Champagne, E. Botek, *Chem. Phys. Lett.* **2009**, *477*, 355–359.

[9] J. Liu, B.-W. Li, Y.-Z. Tan, A. Giannakopoulos, C. Sanchez-Sanchez, D. Beljonne, P. Ruffieux, R. Fasel, X. Feng, K. Müllen, *J. Am. Chem. Soc.* **2015**, *137*, 6097–6103.
[10] J. Liu, X. Feng, *Angew. Chem. Int. Ed.* **2020**, *59*, 23386–23401; *Angew. Chem.* **2020**, *132*, 23591–23607.
[11] S. Mishra, X. Yao, Q. Chen, K. Eimre, O. Gröning, R. Ortiz, M. D. Giovannantonio, J. C. Sancho-García, J. Fernández-Rossier, C. A. Pignedoli, K. Müllen, P. Ruffieux, A. Narita, R. Fasel, *Nat. Chem.* **2021**, *13*, 581–586.
[12] K. Tanaka, S. Yamashita, H. Yamabe, T. Yamabe, *Synth. Met.* **1987**, *17*, 143–148.
[13] X.-Y. Wang, A. Narita, K. Müllen, *Nat. Chem. Rev.* **2017**, *2*, 0100.
[14] X. Feng, W. Pisula, K. Müllen, *Pure Appl. Chem.* **2009**, *81*, 2203–2224.
[15] Z. Qiu, A. Narita, K. Müllen, *Faraday Discuss.* **2021**, *227*, 8–45.
[16] J. Liu, R. Berger, K. Müllen, X. Feng, *From Polyphenylenes to Nanographenes and Graphene Nanoribbons*, Springer, Heidelberg, **2017**, pp. 1–32.
[17] Q. Ye, C. Chi, *Chem. Mater.* **2014**, *26*, 4046–4056.
[18] C. Tönshoff, H. F. Bettinger, *Chem. Eur. J.* **2021**, *27*, 3193–3212.
[19] T. Jousselin-Oba, M. Mamada, K. Wright, J. Marrot, C. Adachi, A. Yassar, M. Frigoli, *Angew. Chem. Int. Ed.* **2021**, *61*, e202112794.
[20] Y. Gu, Y. G. Tullimilli, J. Feng, H. Phan, W. Zeng, J. Wu, *Chem. Commun.* **2019**, *55*, 5567–5570.
[21] W. Zeng, T. Y. Gopalakrishna, H. Phan, T. Tanaka, T. S. Herng, J. Ding, A. Osuka, J. Wu, *J. Am. Chem. Soc.* **2018**, *140*, 14054–14058.
[22] J. Su, M. Telychko, S. Song, J. Lu, *Angew. Chem. Int. Ed.* **2020**, *59*, 7658–7668; *Angew. Chem.* **2020**, *132*, 7730–7740.
[23] S. Song, J. Su, M. Telychko, J. Li, G. Li, Y. Li, C. Su, J. Wu, J. Lu, *Chem. Soc. Rev.* **2021**, *50*, 3238–3262.
[24] W. Chen, F. Yu, Q. Xu, G. Zhou, Q. Zhang, *Adv. Sci.* **2020**, *7*, 1903766.
[25] Z. Sun, Z. Zeng, J. Wu, *Chem. Asian J.* **2013**, *8*, 2894–2904.
[26] W. Zeng, J. Wu, *Chem.* **2021**, *7*, 358–386.
[27] S. Mishra, D. Beyer, K. Eimre, S. Kezilebieke, R. Berger, O. Gröning, C. A. Pignedoli, K. Müllen, P. Liljeroth, P. Ruffieux, X. Feng, R. Fasel, *Nat. Nanotechnol.* **2020**, *15*, 22–28.
[28] S. Mishra, G. Catarina, F. Wu, R. Ortiz, D. Jacob, K. Eimre, J. Ma, C. A. Pignedoli, X. Feng, P. Ruffieux, J. Fernández-Rossier, R. Fasel, *Nature* **2021**, *598*, 287–292.
[29] J. Ma, J. Liu, M. Baumgarten, Y. Fu, Y.-Z. Tan, K. S. Schellhammer, F. Ortmann, G. Cuniberti, H. Komber, R. Berger, K. Müllen, X. Feng, *Angew. Chem. Int. Ed.* **2017**, *56*, 3280–3284; *Angew. Chem.* **2017**, *129*, 3328–3332.
[30] F. Lombardi, J. Ma, D. I. Alexandropoulos, H. Komber, J. Liu, W. K. Myers, X. Feng, L. Bogani, *Chem* **2021**, *7*, 1363–1378.
[31] D.-e. Jiang, S. Dai, *J. Phys. Chem. A* **2008**, *112*, 332–335.
[32] M. Watanabe, K.-Y. Chen, Y. J. Chang, T. J. Chow, *Acc. Chem. Res.* **2013**, *46*, 1606–1615.
[33] H. F. Bettinger, C. Tönshoff, *Chem. Rec.* **2015**, *15*, 364–369.
[34] M. Bendikov, H. M. Duong, K. Starkey, K. N. Houk, E. A. Carter, F. Wudl, *J. Am. Chem. Soc.* **2004**, *126*, 7416–7417.
[35] M. C. dos Santos, *Phys. Rev. B* **2006**, *74*, 045426.
[36] E. Clar, *The Aromatic Sextet*, Wiley, London, **1972**.
[37] Z. Sun, Q. Ye, C. Chi, J. Wu, *Chem. Soc. Rev.* **2012**, *41*, 7857–7889.
[38] A. Konishi, T. Kubo, *Benzenoid Quinodimethanes. Top. Curr. Chem.* **2017**, *375*, 83.
[39] P. Ruffieux, S. Wang, B. Yang, C. Sánchez-Sánchez, J. Liu, T. Dienel, L. Talirz, P. Shinde, C. A. Pignedoli, D. Passerone, T. Dumslaff, X. Feng, K. Müllen, R. Fasel, *Nature* **2016**, *531*, 489–492.
[40] O. Hod, V. Barone, G. E. Scuseria, *Phys. Rev. B* **2008**, *77*, 035411.
[41] D.-e. Jiang, B. G. Sumpter, S. Dai, *J. Chem. Phys.* **2007**, *127*, 124703.
[42] D.-e. Jiang, S. Dai, *Chem. Phys. Lett.* **2008**, *466*, 72–75.
[43] F. Moscardó, E. San-Fabián, *Chem. Phys. Lett.* **2009**, *480*, 26–30.
[44] F. Plasser, H. Pašalić, M. H. Gerzabek, F. Libisch, R. Reiter, J. Burgdörfer, T. Müller, R. Shepard, H. Lischka, *Angew. Chem. Int. Ed.* **2013**, *52*, 2581–2584; *Angew. Chem.* **2013**, *125*, 2641–2644.
[45] A. Shimizu, Y. Hirao, T. Kubo, M. Nakano, E. Botek, B. Champagne, *AIP Conf. Proc.* **2012**, *1504*, 399–405.
[46] K. Yamaguchi, R. Carbo, M. Klobukowski, *Self-Consistent Field: Theory and Applications* (Eds.: R. Carbo, M. Klobukowski), Elsevier, Amsterdam, **1990**, p. 727–823.
[47] S. Yamanaka, M. Okumura, M. Nakano, K. Yamaguchi, *J. Mol. Struct.* **1994**, *310*, 205–218.
[48] R. Scholl, C. Seer, R. Weitzenböck, *Ber. Dtsch. Chem. Ges.* **1910**, *43*, 2202–2209.
[49] E. Clar, *Chem. Ber.* **1948**, *81*, 52–63.
[50] E. Clar, *Chem. Ber.* **1949**, *82*, 46–60.
[51] H. Akamatu, H. Inokuchi, Y. Matsunaga, *Nature* **1954**, *173*, 168–169.
[52] F. Würthner, *Chem. Commun.* **2004**, 1564–1579.
[53] K. Zhang, K.-W. Huang, J. Li, J. Luo, C. Chi, J. Wu, *Org. Lett.* **2009**, *11*, 4854–4857.
[54] A. Bohnen, K. H. Koch, W. Lüttke, K. Müllen, *Angew. Chem. Int. Ed.* **1990**, *29*, 525–527; *Angew. Chem.* **1990**, *102*, 548–550.
[55] T. Weil, T. Vosch, J. Hofkens, K. Peneva, K. Müllen, *Angew. Chem. Int. Ed.* **2010**, *49*, 9068–9093; *Angew. Chem.* **2010**, *122*, 9252–9278.
[56] N. G. Pschirer, C. Kohl, F. Nolde, J. Qu, K. Müllen, *Angew. Chem. Int. Ed.* **2006**, *45*, 1401–1404; *Angew. Chem.* **2006**, *118*, 1429–1432.
[57] A. Konishi, Y. Hirao, M. Nakano, A. Shimizu, E. Botek, B. Champagne, D. Shiomi, K. Sato, T. Takui, K. Matsumoto, H. Kurata, T. Kubo, *J. Am. Chem. Soc.* **2010**, *132*, 11021–11023.
[58] A. Konishi, Y. Hirao, K. Matsumoto, H. Kurata, R. Kishi, Y. Shigeta, M. Nakano, K. Tokunaga, K. Kamada, T. Kubo, *J. Am. Chem. Soc.* **2013**, *135*, 1430–1437.
[59] A. Konishi, Y. Hirao, H. Kurata, T. Kubo, M. Nakano, K. Kamada, *Pure Appl. Chem.* **2014**, *86*, 497–505.
[60] J. Liu, P. Ravat, M. Wagner, M. Baumgarten, X. Feng, K. Müllen, *Angew. Chem.* **2015**, *127*, 12619–12623; *Angew. Chem. Int. Ed.* **2015**, *54*, 12442–12446.
[61] M. Mamada, R. Nakamura, C. Adachi, *Chem. Sci.* **2021**, *12*, 552–558.
[62] M. R. Ajayakumar, Y. Fu, J. Ma, F. Hennersdorf, H. Komber, J. J. Weigand, A. Alfonsov, A. A. Popov, R. Berger, J. Liu, K. Müllen, X. Feng, *J. Am. Chem. Soc.* **2018**, *140*, 6240–6244.
[63] Y. Ni, T. Y. Gopalakrishna, H. Phan, T. S. Herng, S. Wu, Y. Han, J. Ding, J. Wu, *Angew. Chem. Int. Ed.* **2018**, *57*, 9697–9701; *Angew. Chem.* **2018**, *130*, 9845–9849.
[64] M. R. Ajayakumar, Y. Fu, F. Liu, H. Komber, V. Tkachova, C. Xu, S. Zhou, A. A. Popov, J. Liu, X. Feng, *Chem. Eur. J.* **2020**, *26*, 7497–7503.
[65] S. Mishra, T. G. Lohr, C. A. Pignedoli, J. Liu, R. Berger, J. I. Urgel, K. Müllen, X. Feng, P. Ruffieux, R. Fasel, *ACS Nano* **2018**, *12*, 11917–11927.
[66] L. B. Roberson, J. Kowalik, L. M. Tolbert, C. Kloc, R. Zeis, X. Chi, R. Fleming, C. Wilkins, *J. Am. Chem. Soc.* **2005**, *127*, 3069–3075.
[67] X. Zhang, J. Li, H. Qu, C. Chi, J. Wu, *Org. Lett.* **2010**, *12*, 3946–3949.
[68] L. Zöphel, R. Berger, P. Gao, V. Enkelmann, M. Baumgarten, M. Wagner, K. Müllen, *Chem. Eur. J.* **2013**, *19*, 17821–17826.
[69] C. Rogers, C. Chen, Z. Pedramrazi, A. A. Omrani, H. Z. Tsai, H. S. Jung, S. Lin, M. F. Crommie, F. R. Fischer, *Angew. Chem.* **2015**, *127*, 15358–15361; *Angew. Chem. Int. Ed.* **2015**, *54*, 15143–15146.
[70] A. Sánchez-Grande, J. I. Urgel, L. Veis, S. Edalatmanesh, J. Santos, K. Lauwaet, P. Mutombo, J. M. Gallego, J. Brabec, P. Beran, D. Nachtigallová, R. Miranda, N. Martín, P. Jelínek, D. Écija, *J. Phys. Chem. Lett.* **2020**, *12*, 330–336.
[71] J. J. Shen, Y. Han, S. Dong, H. Phan, T. S. Herng, T. Xu, J. Ding, C. Chi, *Angew. Chem. Int. Ed.* **2021**, *60*, 4464–4469; *Angew. Chem.* **2021**, *133*, 4514–4519.
[72] M. R. Ajayakumar, J. Ma, A. Lucotti, K. S. Schellhammer, G. Serra, E. Dmitrieva, M. Rosenkranz, H. Komber, J. Liu, F. Ortmann, M. Tommasini, X. Feng, *Angew. Chem. Int. Ed.* **2021**, *60*, 13853–13858.
[73] X.-Y. Wang, X. Yao, A. Narita, K. Müllen, *Acc. Chem. Res.* **2019**, *52*, 2491–2505.
[74] V. M. Hertz, M. Bolte, H. W. Lerner, M. Wagner, *Angew. Chem. Int. Ed.* **2015**, *54*, 8800–8804; *Angew. Chem.* **2015**, *127*, 8924–8928.
[75] X.-Y. Wang, A. Narita, W. Zhang, X. Feng, K. Müllen, *J. Am. Chem. Soc.* **2016**, *138*, 9021–9024.
[76] T. Katayama, S. Nakatsuka, H. Hirai, N. Yasuda, J. Kumar, T. Kawai, T. Hatakeyama, *J. Am. Chem. Soc.* **2016**, *138*, 5210–5213.
[77] D. Sakamaki, S. Tanaka, K. Tanaka, M. Takino, M. Gon, K. Tanaka, T. Hirose, D. Hirobe, H. M. Yamamoto, H. Fujiwara, *J. Phys. Chem. Lett.* **2021**, *12*, 9283–9292.
[78] X.-Y. Wang, T. Dienel, M. D. Giovannantonio, G. B. Barin, N. Kharche, O. Deniz, J. I. Urgel, R. Widmer, S. Stolz, L. H. D. Lima, M. Muntwiler, M. Tommasini, V. Meunier, P. Ruffieux, X. Feng, R. Fasel, K. Müllen, A. Narita, *J. Am. Chem. Soc.* **2017**, *139*, 4671–4674.
[79] X. Wang, F. Zhang, K. S. Schellhammer, P. Machata, F. Ortmann, G. Cuniberti, Y. Fu, J. Hunger, R. Tang, A. A. Popov, R. Berger, K. Müllen, X. Feng, *J. Am. Chem. Soc.* **2016**, *138*, 11606–11615.
[80] C. R. McConnell, S.-Y. Liu, *Chem. Soc. Rev.* **2019**, *48*, 3436–3453.
[81] Y. Fu, X. Chang, H. Yang, E. Dmitrieva, Y. Gao, J. Ma, L. Huang, J. Liu, H. Lu, Z. Cheng, S. Du, H.-J. Gao, X. Feng, *Angew. Chem. Int. Ed.* **2021**, *60*, 26115–26121.
[82] L. Talirz, P. Ruffieux, R. Fasel, *Adv. Mater.* **2016**, *28*, 6222–6231.
[83] Z. Chen, A. Narita, K. Müllen, *Adv. Mater.* **2020**, *32*, 2001893.

[84] J. Cai, P. Ruffieux, R. Jaafar, M. Bieri, T. Braun, S. Blankenburg, M. Muoth, A. P. Seitsonen, M. Saleh, X. Feng, K. Müllen, R. Fasel, *Nature* **2010**, *466*„ 470–473.
[85] P. Ruffieux, J. Cai, N. C. Plumb, L. Patthey, D. Prezzi, A. Ferretti, E. Molinari, X. Feng, K. Müllen, C. A. Pignedoli, R. Fasel, *ACS Nano* **2012**, *6*, 6930–6935.
[86] P. Han, K. Akagi, F. Federici Canova, H. Mutoh, S. Shiraki, K. Iwaya, P. S. Weiss, N. Asao, T. Hitosugi, *ACS Nano* **2014**, *8*, 9181–9187.
[87] C. Sánchez-Sánchez, T. Dienel, O. Deniz, P. Ruffieux, R. Berger, X. Feng, K. Müllen, R. Fasel, *ACS Nano* **2016**, *10*, 8006–8011.
[88] A. Berdonces-Layunta, J. Lawrence, S. Edalatmanesh, J. Castro-Esteban, T. Wang, M. S. G. Mohammed, L. Colazzo, D. Peña, P. Jelínek, D. G. De Oteyza, *ACS Nano* **2021**, *15*, 5610–5617.
[89] J. Lawrence, A. Berdonces-Layunta, S. Edalatmanesh, J. Castro-Esteban, T. Wang, M. S. G. Mohammed, M. Vilas-Varela, P. Jelinek, D. Peña, D. G. De Oteyza, *arXiv:2107.12754v1*.
[90] J. Li, S. Sanz, N. Merino-Díez, M. Vilas-Varela, A. Garcia-Lekue, M. Corso, D. G. De Oteyza, T. Frederiksen, D. Peña, J. I. Pascual, *Nat. Commun.* **2021**, *12*, 5538.
[91] X. Wang, X. Li, L. Zhang, Y. Yoon, P. K. Weber, H. Wang, J. Guo, H. Dai, *Science* **2009**, *324*, 768–771.
[92] J. Cai, C. A. Pignedoli, L. Talirz, P. Ruffieux, H. Söde, L. Liang, V. Meunier, R. Berger, R. Li, X. Feng, K. Müllen, R. Fasel, *Nat. Nanotechnol.* **2014**, *9*, 896–900.
[93] X.-Y. Wang, J. I. Urgel, G. B. Barin, K. Eimre, M. D. Giovannantonio, A. Milani, M. Tommasini, C. A. Pignedoli, P. Ruffieux, X. Feng, R. Fasel, K. Müllen, A. Narita, *J. Am. Chem. Soc.* **2018**, *140*, 9104–9107.
[94] B. Huang, *Phys. Lett. A* **2011**, *375*, 845–848.
[95] M. Xing, W. Fang, X. Yang, B. Tian, J. Zhang, *Chem. Commun.* **2014**, *50*, 6637–6640.
[96] C. Dou, S. Saito, K. Matsuo, I. Hisaki, S. Yamaguchi, *Angew. Chem. Int. Ed.* **2012**, *51*, 12206–12210; *Angew. Chem.* **2012**, *124*, 12372–12376.
[97] R. R. Cloke, T. Marangoni, G. D. Nguyen, T. Joshi, D. J. Rizzo, C. Bronner, T. Cao, S. G. Louie, M. F. Crommie, F. R. Fischer, *J. Am. Chem. Soc.* **2015**, *137*, 8872–8875.
[98] S. Kawai, S. Saito, S. Osumi, S. Yamaguchi, A. S. Foster, P. Spijker, E. Meyer, *Nat. Commun.* **2015**, *6*, 8098.
[99] N. Friedrich, P. Brandimarte, J. Li, S. Saito, S. Yamaguchi, I. Pozo, D. Peña, T. Frederiksen, A. Garcia-Lekue, D. Sánchez-Portal, J. I. Pascual, *Phys. Rev. Lett.* **2020**, *125*, 146801.
[100] S. Kawai, S. Nakatsuka, T. Hatakeyama, R. Pawlak, T. Meier, J. Tracey, E. Meyer, A. S. Foster, *Sci. Adv.* **2018**, *4*, 10.1126/sciadv.aar7181.
[101] R. E. Blackwell, F. Zhao, E. Brooks, J. Zhu, I. Piskun, S. Wang, A. Delgado, Y.-L. Lee, S. G. Louie, F. R. Fischer, *Nature* **2021**, *600*, 647–652.
[102] B. Cirera, A. Sánchez-Grande, B. de la Torre, J. Santos, S. Edalatmanesh, E. Rodríguez-Sánchez, K. Lauwaet, B. Mallada, R. Zbořil, R. Miranda, O. Gröning, P. Jelínek, N. Martín, D. Ecija, *Nat. Nanotechnol.* **2020**, *15*, 437–443.
[103] B. de la Torre, A. Matěj, A. Sánchez-Grande, B. Cirera, B. Mallada, E. Rodríguez-Sánchez, J. Santos, J. I. Mendieta-Moreno, S. Edalatmanesh, K. Lauwaet, M. Otyepka, M. Medveď, Á. Buendía, R. Miranda, N. Martín, P. Jelínek, D. Écija, *Nat. Commun.* **2020**, *11*, 4567.
[104] A. Sánchez-Grande, J. I. Urgel, A. Cahlík, J. Santos, S. Edalatmanesh, E. Rodríguez-Sánchez, K. Lauwaet, P. Mutombo, D. Nachtigallová, R. Nieman, H. Lischka, B. de la Torre, R. Miranda, O. Gröning, N. Martín, P. Jelínek, D. Écija, *Angew. Chem. Int. Ed.* **2020**, *59*, 17594–17599; *Angew. Chem.* **2020**, *132*, 17747–17752.

Manuscript received: November 25, 2021
Revised manuscript received: February 7, 2022
Accepted manuscript online: February 9, 2022